Title: Dynamics of viscoelastic liquid filaments: Low capillary number flows

Authors: Pradeep P. Bhat, Osman A. Basaran, Matteo Pasquali

PII: S0377-0257(07)00232-7
DOI: doi:10.1016/j.jnnfm.2007.10.021
Reference: JNNFM 2783

To appear in: *J. Non-Newtonian Fluid Mech.*

Received date: 19-8-2007
Revised date: 19-10-2007
Accepted date: 19-10-2007

Please cite this article as: P.P. Bhat, O.A. Basaran, M. Pasquali, Dynamics of viscoelastic liquid filaments: Low capillary number flows, *Journal of Non-Newtonian Fluid Mechanics* (2007), doi:10.1016/j.jnnfm.2007.10.021

Dynamics of viscoelastic liquid filaments: low capillary number flows

Pradeep P. Bhat [a], Osman A. Basaran [b], Matteo Pasquali [a,*]

[a] *Department of Chemical and Biomolecular Engineering, and Computer and Information Technology Institute, Rice University, Houston, TX 77005, USA*

[b] *School of Chemical Engineering, Purdue University, West Lafayette, IN 47907, USA*

Abstract

Many applications of viscoelastic free surface flows requiring formation of drops from small nozzles, e.g., ink-jet printing, micro-arraying, and atomization, involve predominantly extensional deformations of liquid filaments. The capillary number, which represents the ratio of viscous to surface tension forces, is small in such processes when drops of water-like liquids are formed. The dynamics of extensional deformations of viscoelastic liquids that are weakly strain hardening, i.e., liquids for which the growth in the extensional viscosity is small and bounded, are here modeled by the Giesekus, FENE-P, and FENE-CR constitutive relations and studied at low capillary numbers using full 2-D numerical computations. A new computational algorithm using the general conformation tensor based constitutive equation [J. Non-Newtonian Fluid Mech., 120:101–135, 2004.] to compute the time dependent viscoelastic free surface flows is presented. DEVSS-TG/SUPG mixed finite element method [J. Non-Newtonian Fluid Mech., 108:363–409, 2002.] is used for the spatial discretization and a fully implicit second-order predictor-corrector scheme is used for the time integration. Inertia, capillarity, and viscoelasticity are incorporated in the computations and the free surface shapes are computed along with all the other field variables in a fully coupled way. Among the three models, Giesekus filaments show the most drastic thinning in the low capillary number regime. The dependence of the transient Trouton ratio on the capillary number in the Giesekus model is demonstrated. The elastic unloading near the end plates is investigated using both kinematic [J. Non-Newtonian Fluid Mech., 79:469–501, 1998.] and energy analyses. The magnitude of elastic unloading, which increases with growing elasticity, is shown to be the largest for Giesekus filaments, thereby suggesting that necking and elastic unloading are related.

Key words: Filament stretching; Drop breakup; Viscoelastic flow; Elastic recoil; Ink-jet printing

1 Introduction

Applications involving fluid flow with deformable liquid-gas interfaces, which is a type of free surface flow, of non-Newtonian liquids are ubiquitous in industries and households. Deposition of thin film coatings on solid substrates and formation of drops out of nozzles are the two commonest examples. Surface coating is used in the production of some of the everyday use products such as tapes, adhesives, and CDs [1]. Drop formation is used in applications such as ink-jet printing [2], micro-arraying [3], and atomization [4]. Production of drops in these applications generally involves deformation of liquid filaments that form out of nozzles at length scales of a few micrometers and time scales of a few microseconds. For example, in drop-on-demand (DOD) ink-jet printing, typically, drops of few tens of micrometers radii are produced in 100 μs or less (see, e.g., [5] for production of water drops). The capillary number, $Ca \equiv \eta_0 U_b/\gamma$, where η_0 is the liquid viscosity, γ is the surface tension, and U_b is the bulk liquid velocity (typically a few hundreds of cm/s in DOD ink-jet printing [5]), in this process is small (< 1) for water-like liquids. Examples of non-Newtonian drop production from small nozzles can be found in [6], in which, the authors report dripping experiments with polyethylene oxide (PEO) solutions that have viscosity of about 6 mPa·s (6 times that of water) and surface tension of about 62 mN/m (0.86 times that of water). Assuming U_b to be 100 cm/s, the capillary number associated with the production of drops of this liquid using DOD ink-jet printing would be $Ca = (0.006 \times 1)/(0.062) \sim 0.1$. In dripping type applications, Ca would be still smaller, because U_b in dripping is much smaller than that in ink-jet printing. Whereas the dynamics of Newtonian liquid filaments is fairly well understood in such flows, an improved understanding of non-Newtonian dy-

* Corresponding author. Tel +1 713 348 5830; Fax +1 713 348 5478. *Email:* mp@rice.edu (M. Pasquali).

Email addresses: pbhat@purdue.edu (Pradeep P. Bhat), obasaran@purdue.edu (Osman A. Basaran).

namics is needed [2, 7] and is a goal of this paper.

There are several methods to produce drops from nozzles (see [2] for a recent review). In all these methods, essentially, an elongating liquid filament or a liquid bridge is formed connecting two 'blobs' or reservoirs of the liquid. This filament subsequently thins or necks by capillary action or by externally applied strain and breaks forming individual drops. Formation of drops thus involves predominantly extensional deformation. The material property which characterizes the resistance of the liquid to such stretching or uni-axial extensional deformation is the (uni-axial) extensional viscosity, $\eta_{\text{E}} = (T_{zz} - T_{rr}) \,/\, \dot{\varepsilon}$, where T_{zz} is the axial stress, T_{rr} is the radial stress, and $\dot{\varepsilon}$ is the elongation rate. η_{E} for a Newtonian liquid is a constant and is simply three times its shear viscosity [8]. However, for viscoelastic liquids the extensional viscosity is not a constant, but is a function of both the rate of strain and the total strain accumulated. The viscoelastic effects due to the extensional viscosity are well manifested by the delay in the capillary breakup of the filaments and, in some cases, the eventual formation of the 'beads on a string' morphology (i.e., many droplets of the liquid which are inter-connected by strands of the liquid) [9, 10]. For the sake of brevity, hereafter the uni-axial extensional viscosity is called simply extensional viscosity.

Kinetic theory based viscoelastic models incorporating finite extensibility of the polymer molecules (e.g., FENE dumbbells [11]) show bounded growth of the extensional viscosity with strain. Such models are called *weakly strain hardening* models when the growth of the extensional viscosity is small. The extent of strain hardening in these models is controlled by the model parameters. Incorporation of finite extensibility has been shown to be important in predicting the terminal thinning regime and eventual breakup of the polymeric liquid filaments [12]. This class of viscoelastic models is used in the present analysis.

Over the past two decades several extensional rheometers have been developed to measure the extensional viscosity of polymer solutions [13–16]. Among them, the filament stretching extensional rheometers (FISERs) pioneered by Matta and Tytus [17] and Sridhar *et al.* [18] have been shown to be the most reliable instruments. In a FISER, a vertical column of the liquid held between two circular plates, i.e., a liquid bridge, is stretched by moving either the top or the bottom plate. The plates are separated exponentially in time and the rate of stretching $\dot{\varepsilon}$ is kept constant in order to mimic uni-axial elongation. Thinning of the filament in the mid-plane is recorded using a laser micrometer or a high speed camera, and the force on the stationary plate is measured to obtain the transient growth of the stress in the filament. The evolution of the mid-filament radius and the stress are then used to determine the extensional viscosity [19, 20].

Stresses that develop in FISERs are inhomogeneous, although uni-axial elongation is what is desired. Stresses inside the filaments are not directly measurable and numerical computations are needed to study and quantify the development of inhomogeneous stress profiles in FISERs [21–24]. Moreover, the dynamics of stretching and the eventual breakup of liquid filaments in FISER devices is similar to the formation and pinch-off of drops [25]. Numerical studies of stretching liquid filaments are thus useful in the analysis of FISER data and in understanding better the drop formation and pinch-off process.

Numerical studies of dynamics of weakly strain hardening liquids in FISER type flow problems have been conducted by Yao *et al.* [26, 27] (at Ca = 9.44, 19.7, and ∞), Kolte *et al.* [22] ($Ca = \infty$), and Matallah *et al.* [28] (Ca = 1, 2, 10, and ∞)—all at capillary number greater than or equal to one. Yao *et al.* have shown that weakly strain hardening models—Giesekus [29] and FENE-P [11]—dramatically depart from the Newtonian behavior by exhibiting a cohesive *necking failure*, i.e., these filaments exhibit a faster breakup

compared to their Newtonian counterpart with the same *Ca*. Necking failure in viscoelastic filaments modeled by the Papanastasiou-Scriven-Macosko (PSM) model [30], in the absence of surface tension, has been studied by Hassager *et al.* [31]. Foteinopoulou *et al.* have studied the growth of an axisymmetric bubble inside an elongating viscoelastic filament [32], and the growth of single and multiple bubbles inside Newtonian filaments [32, 33].

In free surface flow computations, the location of the liquid-gas interface is unknown *a priori* and its solution is a part of the complete solution. Many interface-tracking methods, e.g., boundary element (BEM) [34, 35], volume-of-fluid (VOF) [36], and level set methods [37], are available to compute the free surface shapes. While all of these methods can follow large interface deformations, each has some limitation. Although highly accurate, BEM does not lend itself readily to situations in which the governing equations are nonlinear. Diffuse interface and interface capturing methods such as VOF and level sets are extremely flexible and easy to use but are not as accurate as techniques in which the interface is tracked, as in BEM and the approach that is described below and adopted here. The finite element method (FEM) has been demonstrated to be a highly accurate method for computation of Newtonian free surface flows [38–43]. Moreover, FEM algorithms in which the locations of free boundaries are computed coupled with the solutions of the conservation equations, while more difficult to implement than VOF and level set algorithms, have been demonstrated to capture large free surface deformations and interface pinch-off in situations where surface tension effects are significant [43–45].

FEM has also been extended successfully to solve viscoelastic flows and many stable algorithms have been developed to handle the additional nonlinearity introduced by the viscoelastic constitutive equations (see [46, 47] for reviews). Viscoelastic free surface flow calculations with different methods of handling free boundaries have been presented more recently [48–55]. A

new, fully-coupled (i.e., all variables, including free surface shapes, are solved simultaneously) transient algorithm based on the DEVSS-TG/SUPG finite element method [49] with conformation tensor based constitutive models is presented here.

In this article three weakly strain hardening models, Giesekus, FENE-CR [56], and FENE-P, are used in analyzing the dynamics of a filament stretching setup at low *Ca*. Section 2 contains the description of the governing equations, the problem, and the relevant dimensionless parameters in this setup. Section 3 contains the details of the numerical method, and Section 4 presents the computational results with a detailed analysis. Key findings of the paper are summarized in Section 5.

2 Governing physics

2.1 Transport equations

The conservation equations of mass (for incompressible flow) and momentum are

$$0 = \boldsymbol{\nabla} \cdot \mathbf{v} \tag{1}$$

$$\rho \frac{\partial \mathbf{v}}{\partial t} = -\rho \mathbf{v} \cdot \boldsymbol{\nabla} \mathbf{v} + \boldsymbol{\nabla} \cdot \mathbf{T} + \boldsymbol{\nabla} \Theta \tag{2}$$

where ρ is the density of the liquid, $\mathbf{v}$ is the velocity, $\mathbf{T}$ is the Cauchy stress tensor, Θ is the potential of body force per unit volume, $\boldsymbol{\nabla} \equiv \frac{\partial}{\partial \mathbf{x}}$ is the usual spatial gradient, and $\frac{\partial}{\partial t}$ is the partial time derivative. The stress tensor $\mathbf{T}$ is split into an isotropic part, a viscous part, and an elastic part as

$$\mathbf{T} = -p\mathbf{I} + \boldsymbol{\tau} + \boldsymbol{\sigma} \tag{3}$$

where p is the pressure, $\mathbf{I}$ is the identity tensor, $\boldsymbol{\tau}$ is the viscous stress tensor and $\boldsymbol{\sigma}$ is the polymer contribution to the Cauchy stress or the elastic stress tensor. The viscous stress tensor $\boldsymbol{\tau}$ is defined by the Newton's law of viscosity:

$$\boldsymbol{\tau} = 2\eta_s \mathbf{D} \tag{4}$$

where η_s is the solvent viscosity and $\mathbf{D} = \frac{1}{2}[\boldsymbol{\nabla}\mathbf{v} + (\boldsymbol{\nabla}\mathbf{v})^T]$ is the rate of strain tensor.

The polymer contribution to the Cauchy stress is modeled by the general conformation tensor based constitutive equation [49]. Microstructural features of polymer solutions can be represented by a single variable, the conformation tensor [57–60], which gives the expectation values of the local microstructural features. The transport equation for the dimensionless conformation tensor $\mathbf{M}$ in an isothermal flow, neglecting diffusion, can be written as [57]

$$\begin{aligned}\frac{\partial \mathbf{M}}{\partial t} = &-\mathbf{v}\cdot\boldsymbol{\nabla}\mathbf{M} + 2\xi\frac{\mathbf{D}{:}\mathbf{M}}{\mathbf{I}{:}\mathbf{M}}\mathbf{M} + \zeta(\mathbf{M}\cdot\mathbf{D} + \mathbf{D}\cdot\mathbf{M} - 2\frac{\mathbf{D}{:}\mathbf{M}}{\mathbf{I}{:}\mathbf{M}}\mathbf{M}) \\ &+\mathbf{M}\cdot\mathbf{W} + \mathbf{W}^T\cdot\mathbf{M} - \frac{1}{\lambda}(g_0\mathbf{I} + g_1\mathbf{M} + g_2\mathbf{M}^2)\end{aligned} \tag{5}$$

where $\mathbf{W} = \frac{1}{2}[\boldsymbol{\nabla}\mathbf{v} - (\boldsymbol{\nabla}\mathbf{v})^T]$ is the vorticity tensor, λ is the characteristic relaxation time of the polymer, $\xi(\mathbf{M})$, $\zeta(\mathbf{M})$, $g_0(\mathbf{M})$, $g_1(\mathbf{M})$, and $g_2(\mathbf{M})$ are constitutive functions whose forms depend on the type of the constitutive relation chosen. Table 1 lists the forms of these functions in the different constitutive relations used in this paper.

The elastic stress tensor is obtained from the conformation tensor $\mathbf{M}$ as [49]

$$\boldsymbol{\sigma} = 2(\xi - \zeta)\frac{(\mathbf{M} - \mathbf{I})}{\mathbf{I}{:}\mathbf{M}}\mathbf{M}{:}\frac{\partial a}{\partial \mathbf{M}} + 2\zeta\,(\mathbf{M} - \mathbf{I})\cdot\frac{\partial a}{\partial \mathbf{M}} \tag{6}$$

where $a\,(\mathbf{M})$ is the Helmholtz free energy per unit volume.

2.2 Problem description and boundary conditions

Figure 1 shows a schematic of an axisymmetric liquid bridge being stretched between a moving top plate and a stationary bottom plate with equal radii.

The slenderness is defined by the bridge initial aspect ratio $\Lambda_0 = L_0/R_0$ where L_0 is the initial height of the liquid column and R_0 is the radius of the plate. The evolution of the stress fields in the liquid column depends on its slenderness; thicker bridges display less homogeneous stress fields during the initial stages of stretching for Boger type liquids [23]. Hereafter, $\Lambda_0 = 3$ unless stated otherwise.

The stretching of the filaments results in their straining. In the *exponential* stretching, the resulting Hencky strain is

$$\varepsilon = \dot{\varepsilon}\, t \tag{7}$$

The no slip condition at the end plates causes filaments with curved surfaces. Excessive deformation due to this curved nature of the filaments is quantified by the effective strain [26]:

$$\varepsilon_{\text{eff}} = 2 \ln \left(\frac{R_0}{R_{\text{mid}}} \right) \tag{8}$$

where R_{mid} is the mid-plane filament radius. In this study, exponential stretching of filaments is computed unless stated otherwise.

The boundary conditions on the transport equations are as follows.

- Along the top plate, $\partial\Omega_{\mathfrak{t}}$: Adherence and no slip, i.e., $v_z = v_z(t)$, and $v_r = 0$, where v_z is the axial and v_r is the radial component of velocity. In the exponential stretching, the length of the bridge at any instant t is $L(t) = L_0 e^{\dot{\varepsilon} t}$, which implies $v_z(t) = \dot{\varepsilon}\, L_0 e^{\dot{\varepsilon} t}$, thus mimicking the uni-axial

elongational flow [23]. In the linear stretching, $L(t) = L_0 + Ut$ and therefore, $v_z(t) = U$, where U is constant.

- Along the bottom plate, $\partial\Omega_{\rm b}$: No slip and no penetration, i.e., $\mathbf{v} = \mathbf{0}$.
- Along the axis of symmetry, $\partial\Omega_{\rm s}$: No penetration, i.e., $\mathbf{n}\cdot\mathbf{v} = 0$, and vanishing shear stress, i.e., $\mathbf{tn} : \mathbf{T} = 0$, where $\mathbf{n}$ is the unit normal, and $\mathbf{t}$ is the unit tangent to the boundary.
- Along the free surface, $\partial\Omega_{\rm f}$: The force balance across the interface is applied through the traction boundary condition:

$$\mathbf{n}\cdot\mathbf{T} = -p_{\rm amb}\,\mathbf{n} + (2H\gamma)\mathbf{n} \tag{9}$$

where $p_{\rm amb}$ is the ambient pressure (i.e., in the gas phase), γ is the surface tension of the liquid-gas interface, and H is the mean curvature.

The initial condition for computations is that of a cylindrical liquid column at rest with no extra stresses: $\mathbf{v} = \mathbf{0}$, $p = 0$, $\mathbf{L} = \mathbf{0}$, and $\mathbf{M} = \mathbf{I}$, i.e., $\boldsymbol{\sigma} = \mathbf{0}$.

2.3 Dimensionless numbers

The dynamics of stretching viscoelastic filaments is governed by the following dimensionless numbers: Reynolds number, $Re \equiv \rho\tilde{U}\tilde{L}/\eta_0$, where $\tilde{U}$ is the characteristic velocity and $\tilde{L}$ is the characteristic length of the flow; capillary number, $Ca \equiv \eta_0\tilde{U}/\gamma$; Bond number, $Bo \equiv \rho g\tilde{L}^2/\gamma$, where g is the acceleration due to gravity; viscosity ratio, $\beta \equiv \eta_s/\eta_0$, and Deborah number, $De \equiv \lambda/\tilde{t}$, where $\tilde{t}$ is the characteristic process time of the flow. Re represents the ratio of inertial to viscous forces, Ca represents the ratio of viscous to surface tension forces, Bo represents the ratio of gravity to surface tension forces, β gives the solvent contribution to the total viscosity, and De represents the ratio of polymer relaxation time to the characteristic flow time. In the exponential separation of plates, the characteristic time is $\tilde{t} = (\dot{\varepsilon})^{-1}$, the characteristic length is $\tilde{L} = R_0$, and the characteristic velocity is $\tilde{U} = R_0\,\dot{\varepsilon}$. In the linear

separation of plates at a constant speed U, the characteristic time is $\tilde{t} = R_0/U$, the characteristic length is $\tilde{L} = R_0$, and the characteristic velocity is $\tilde{U} = U$.

The resulting dimensionless numbers for the exponential plate separation are

$$Re = \frac{\rho\, \dot{\varepsilon}\, R_0^2}{\eta_0} \tag{10}$$

$$Ca = \frac{\eta_0\, \dot{\varepsilon}\, R_0}{\gamma} \tag{11}$$

$$Bo = \frac{\rho g R_0^2}{\gamma} \tag{12}$$

$$De = \lambda\, \dot{\varepsilon} \tag{13}$$

$$\beta = \frac{\eta_s}{\eta_0} \tag{14}$$

Hereafter, gravity is neglected ($Bo = 0$) unless stated otherwise.

In addition to these dimensionless numbers, viscoelastic model parameters (listed in Table 1) also affect the dynamics of filaments.

3 Numerical method

3.1 Mesh equation

The elliptic mapping method of de Santos [61] is used here to compute the flow domain and the moving boundary. The elements in the physical domain are mapped onto a reference element in the computational domain; position in the reference domain $\boldsymbol{\xi}$ is given by the mapping $\boldsymbol{\xi} = \boldsymbol{\xi}(\mathbf{x})$, where $\mathbf{x}$ is the position in the physical domain. The elliptic method requires such a mapping to obey the following elliptic differential equation:

$$\mathbf{0} = \boldsymbol{\nabla} \cdot \left(\tilde{\mathbf{D}} \cdot \boldsymbol{\nabla} \boldsymbol{\xi} \right) \tag{15}$$

where the dyadic $\tilde{\mathbf{D}}$ controls the spacing of the co-ordinate lines. Solution of Eq. 15 gives the mapping $\boldsymbol{\xi}$; position in the physical domain $\mathbf{x}$ is then obtained from the inverse mapping $\mathbf{x} = \mathbf{x}(\boldsymbol{\xi})$.

Equation 15 is solved using the following boundary conditions: (1) the nodes at the stationary bottom plate ($\partial\Omega_{\mathrm{b}}$) are fixed; (2) the radial positions of the nodes at the top plate ($\partial\Omega_{\mathrm{t}}$) are held fixed and their axial positions are subjected to the same translation as the plate, i.e., $z = L(t)$; (3) the co-ordinate lines are held orthogonal to one another along the line of symmetry ($\partial\Omega_{\mathrm{s}}$), i.e., $\mathbf{n}\cdot\boldsymbol{\nabla}\boldsymbol{\xi} = \mathbf{0}$; and (4) the component of the mapping that aligns with the normal to the free surface ($\partial\Omega_{\mathrm{f}}$) is subjected to the kinematic boundary condition:

$$0 = \mathbf{n}\cdot(\mathbf{v} - \mathbf{v}_s) \tag{16}$$

where $\mathbf{v}_s$ is the velocity of points on the boundary, and the nodes are distributed uniformly in the tangential direction (i.e., along the free surface). Conditions (1) and (2) also ensure that the two contact lines remain fixed or pinned to the sharp edges of the two plates.

The movement of the mesh in a time dependent flow computation is accounted for by transforming the partial time derivative of any physical quantity Φ as

$$\frac{\partial\Phi}{\partial t} = \mathring{\Phi} - \mathring{\mathbf{x}}\cdot\boldsymbol{\nabla}\Phi \tag{17}$$

where $\mathring{\Phi}$ is the time derivative of Φ in a fixed frame and $\mathring{\mathbf{x}}$ is the mesh velocity.

3.2 Spatial discretization

We use DEVSS-TG/SUPG finite element method [49, 62, 63] to discretize the mapping and transport equations. DEVSS-TG involves the introduction of the following additional equation whose solution gives the interpolated traceless velocity gradient $\mathbf{L}$ [49]:

$$\mathbf{0} = \mathbf{L} - \boldsymbol{\nabla}\mathbf{v} + \frac{1}{\operatorname{tr}\mathbf{I}}(\boldsymbol{\nabla}\cdot\mathbf{v})\mathbf{I} \tag{18}$$

where $\operatorname{tr}\mathbf{I}$ is the trace of $\mathbf{I}$. The rate of strain tensor and the vorticity tensor are then obtained as

$$\mathbf{D} = \frac{1}{2}(\mathbf{L} + \mathbf{L}^T) \;\text{ and }\; \mathbf{W} = \frac{1}{2}(\mathbf{L} - \mathbf{L}^T) \tag{19}$$

The viscous stress tensor is [49]

$$\boldsymbol{\tau} = \eta_s(\mathbf{L} + \mathbf{L}^T) + \eta_a[\boldsymbol{\nabla}\mathbf{v} + (\boldsymbol{\nabla}\mathbf{v})^T - \mathbf{L} - \mathbf{L}^T] \tag{20}$$

where η_a is a numerical parameter whose value is of the same order as that of η_0.

DEVSS-TG/SUPG is a mixed finite element method. We use biquadratic continuous basis functions for velocity $\mathbf{v}$ and mapping $\boldsymbol{\xi}$, linear discontinuous basis functions for pressure p (see, e.g., p. 354 in [64]), and bilinear continuous basis functions for interpolated velocity gradient $\mathbf{L}$ and conformation tensor $\mathbf{M}$.

3.3 Time integration

A fully implicit predictor-corrector time integration with adaptive stepping is used here [65, 66]. First- and second-order finite differences are used for the

temporal discretizations.

A few (typically 4) first-order forward Euler predictor and backward Euler corrector steps with constant step size Δt are carried out initially to get the necessary smoothing [67] before switching to second-order Adams-Bashforth predictor and trapezoid-rule corrector steps. Time step size for the $(n+1)^{\text{th}}$ computational step is obtained adaptively from the n^{th} step as

$$\Delta t_{n+1} = \Delta t_n \left(\frac{\delta}{||d_n||} \right)^{1/3} \tag{21}$$

where δ is the relative-error tolerance (here in the range 0.001–0.005) and d_n is the local truncation error given by the following relation:

$$d_n = \frac{\mathbf{y}_{n+1} - \mathbf{y}^p_{n+1}}{3\left(1 + \frac{\Delta t_{n-1}}{\Delta t_n}\right)} \tag{22}$$

where $\mathbf{y}_{n+1}$ is the corrected solution and $\mathbf{y}^p_{n+1}$ is the predicted solution.

The algebraic equations resulting from these discretizations are solved using Newton's method with an analytical Jacobian. The linear algebra solver is based on the frontal algorithm of Duff *et al.* [68].

3.4 Remeshing

Necking and elongation of the filaments at high strains result in the distortion and lower density of elements in the region of high stresses. To preserve accuracy, we halt our calculations when a critical criterion for mesh quality is violated. Elements are then added and redistributed. Time marching is then continued with the fine mesh.

The coarse mesh data are saved at two successive time steps just before halting the calculations. These data are then projected onto a fine mesh, and

time derivatives are calculated. Calculations are then restarted using first-order Euler for the first four time steps, after which the second-order schemes are used.

The projection of the coarse mesh data onto a fine mesh is carried out first by locating the fine mesh nodes in an undistorted coarse mesh. The field variables ($\mathbf{x}$, $\mathbf{v}$, p, $\mathbf{L}$, and $\mathbf{M}$) are then interpolated. Because position $\mathbf{x}$ is also interpolated, a boundary fitted mesh is obtained; thus, free surface deformations are automatically accounted for.

4 Results and discussion

4.1 Method validation

The computational method is tested first by simulating an evolving Newtonian filament with an initial aspect ratio of 3. The upper plate is moved at a constant speed, and the dimensionless numbers are $Re = 9.56$, $Ca = 8.2\times10^{-5}$, and $Bo = 0.342$. Same dimensionless numbers were used by Zhang *et al.* (ZPB) [25] in their 1-D analysis of and experiments on stretching Newtonian liquid bridges. Table 2 contains the comparisons of the breakup length L_b/R_0 and the ratio (%) of the volume of the sessile drop to the total volume V_{sessile}/V between the present work (2-D) and that of ZPB. For a minimum neck radius $R_{\min}/R_0 = 5.5\times10^{-3}$, L_b/R_0 agrees within 0.82% of ZPB and V_{sessile}/V agrees within 0.49% of ZPB.

When the simulation is continued further, i.e., for $R_{\min}/R_0 < 5.5\times10^{-3}$, the liquid-gas interface in the neck region close to breakup *overturns*. Such overturning of interfaces in the neck region of Newtonian drops at these dimensionless numbers has been predicted by Wilkes *et al.* [42] and then experimentally confirmed by Notz *et al.* [69] and Chen *et al.* [43]. Figure 2 shows

the overall filament profile and a close-up of the overturned interface. The free surface is multi-valued for a given axial location in the overturned region; this feature can not be captured by 1-D computations.

The method is further tested by comparing the results from the simulation of a stretching Oldroyd-B filament with that of Yao and McKinley (YM) [23]. The upper plate is moved such that the plates are separated exponentially in time. The dimensional numbers are $\Lambda_0 = 1/3$, $Re = 0.0138$, $Ca = 63.26$, $Bo = 0$, and $\beta = 0.915$ as in YM. Figure 3 shows the comparison of the evolution of the minimum neck radius $R_{\min}/R_0$ with the Hencky strain ε. The data from YM are obtained from Fig. 7 of [23] using the `datathief` (NIKHEF-K) tracing software. Our calculations show good agreement with that of YM for different elasticities studied ($De = 0$, 0.5, and 1.0); however, in the case of $De = 0.5$ at $\varepsilon > 4$, a difference of about 6% is found between the two results. We see much smaller difference in other comparisons (a comparison of our calculations of thinning in Giesekus filaments with that in [26] will be shown subsequently). Figure 4 shows the comparisons of the calculated axial velocity normalized with the upper plate velocity, v_z/U, along the axis of symmetry with that of YM at a higher elasticity ($De = 5.01$). Our calculations agree well with YM.

Figure 5 shows the contour plots of the axial component of the conformation tensor M_{zz} at $\varepsilon = 1.62$. It can be seen that a thin boundary layer in M_{zz} has developed near the free surface in the mid-filament region. This agrees well with YM's observation of axial stress boundary layers near the free surface at these strains. For the Oldroyd-B constitutive relation, a boundary layer in M_{zz} indicates a boundary layer in the axial elastic stress σ_{zz}, because the conformation tensor $\mathbf{M}$ and the elastic stress tensor $\boldsymbol{\sigma}$ are proportional ($\boldsymbol{\sigma} = G(\mathbf{M} - \mathbf{I})$). Thus, in effect we also see boundary layers in elastic stress near the free surface. YM showed that filaments that are initially more slender (i.e., higher Λ_0) yield less steep boundary layers. Our calculations with different Λ_0

confirm this observation (not shown).

4.2 Mesh and time step convergence tests

The method is tested for mesh and time step convergence and the respective orders of convergence are obtained using Richardson extrapolation [70]:

$$f(h_e) = f(0) + Ch_e^{\chi} \tag{23}$$

where f is any computed variable expressed as a function of the characteristic element size h_e, $f(0)$ is the extrapolated value at infinitely small element size, C is a constant, and χ is the order of convergence. The problem of an evolving Giesekus filament with parameters same as in [26] (i.e., $\Lambda_0 = 0.54$, $Re = 0$, $Ca = 18.27$, $\beta = 0.262$, $\alpha = 0.32$, and $De = 2$) is solved. Two variables, the minimum neck radius $R_{\min}/R_0$ and the extensional component of the conformation tensor, M_{zz}, along the free surface are tracked. They are then used to compute the orders of convergence.

4.2.1 Mesh convergence

Three meshes, Mesh 1, Mesh 2, and Mesh 3, are used. Mesh 1 has 6 radial and 67 axial elements; Mesh 2 has 9 radial and 100 axial elements; and Mesh 3 has 14 radial and 150 axial elements (the characteristic element size h_e in these meshes decreases progressively by a factor of 1.5).

Simulations are conducted up to Hencky strain of 3 (as in [26]) using a constant time step size (10^{-3}). Figure 6 shows the variation of M_{zz} along the free surface at $\varepsilon = 3$. Curves from computations with the three meshes overlap except at the center of the filament where the peak in M_{zz} lies. The inset in the figure shows the detail near the peak; clearly, results converge with mesh refinement as is expected from any grid-based computational method.

The calculated value of the minimum neck radius $R_{\min}/R_0$ and the maximum in M_{zz} along the free surface, $(M_{zz})_{\max}$, obtained with the three meshes at $\varepsilon = 3$ are tabulated in Table 3. The order of mesh convergence is then calculated using Richardson extrapolation; good orders of 3.65, and 3.07, are obtained from $R_{\min}/R_0$, and $(M_{zz})_{\max}$, respectively.

Figure 7 shows the variation of the relative error with the characteristic element size h_e in $R_{\min}/R_0$ (Fig. 7 (a)) and $(M_{zz})_{\max}$ (Fig. 7 (b)). The relative error in the calculation of a variable $f(h_e)$ is $|f(h_e) - f(0)|/f(0)$. As expected, the error in the computation tends to zero as $h_e \to 0$.

4.2.2 Time step convergence

The time integration scheme used in this work is second-order accurate; therefore, the order of time step convergence is expected to be 2. This is verified by conducting simulations with three fixed time steps: $\Delta t_1 = 2 \times 10^{-3}$, $\Delta t_2 = 1 \times 10^{-3}$, and $\Delta t_3 = 5 \times 10^{-4}$ (each successive time step smaller by a factor of 2). Mesh 2 (described before) is used in the computations and Richardson extrapolation is used to obtain the order of convergence.

The minimum neck radius $R_{\min}/R_0$ and $(M_{zz})_{\max}$ along the free surface obtained from computations with the three time steps at $\varepsilon = 3$ are tabulated in Table 4. An order of convergence of 2.06 is obtained from both of these results; thus, the method is second-order accurate as expected.

The equivalence of results from adaptive and fixed time step calculations is verified next. Minimum neck radius from two simulations, one with adaptive steps and the other with a fixed step ($\Delta t = 10^{-3}$), are compared. The same mesh (Mesh 2) is used in these simulations.

Figure 8 shows the calculated variation of the minimum neck radius $R_{\min}/R_0$ with Hencky strain ε from the two simulations. Clearly, results from

the two simulations agree well. Whereas with the fixed Δt, a total of 1500 simulation time steps are required to reach $\varepsilon = 3$ at a stretch rate $\dot{\varepsilon} = 2$, only 68 steps are used in the adaptive time stepping method (same $\dot{\varepsilon}$ and an average time step size of 2.2×10^{-2}). Thus, computations with adaptive steps are much faster. Yao *et al.*'s [26] results are also included for comparison; the figure makes plain that our calculations agree well with their results.

4.3 Dynamics of weakly strain hardening liquid filaments

4.3.1 Capillary effects on Giesekus filaments

Yao *et al.* [26, 27] have studied the dynamics of stretching Giesekus filaments with parameters obtained from the experimental characterization of 5 wt% polystyrene solution in tricresyl phosphate and dioctyl phthalate [71]. Their calculations were carried out at high Ca (≥ 9.44) and small initial aspect ratios. They found that Giesekus filaments undergo a drastic necking failure by showing a faster thinning compared to their Newtonian counterparts at the same Ca. They maintain that their observations were insensitive to Ca by showing that the evolution of the extensional viscosity does not depend upon Ca. In this paper, the effect of lowering Ca further on the dynamics of these filaments is investigated. The effects of inertia are removed by setting $Re = 0$ (creeping flow). Inertial effects become important only in the vicinity of breakup of the filament when the outer fluid has negligible viscosity [35].

The effects of varying the mobility parameter α on the dynamics of the filaments have been studied [23]. As α is decreased, the resistance to stretching is enhanced, and the filament thins slower. The Oldroyd-B model, which predicts that filament breakup does not occur in finite time [72], is recovered when $\alpha = 0$. Two sets of (α, β) values are used in this paper. In studying the effect of lowering Ca on the evolution of the minimum neck radius, α is set to

0.32 and β is set to 0.262 as in [26]. In all the subsequent studies, α is set to 0.1 and β is set to 0.6 so that sufficient contribution from the polymer to the total viscosity is maintained.

Figure 9 shows the thinning of Giesekus and Newtonian filaments with Hencky strain ε at different Ca. The necking in the Giesekus filaments grows more *rapidly* when compared with their Newtonian counterparts at all Ca, and it can be seen that the deviation from the Newtonian behavior in the Giesekus filaments starts *earlier* as Ca is decreased. The earlier non-linear analysis of the stability of the viscoelastic liquid filaments to surface tension driven deformations shows that the growth of perturbations in Oldroyd-B filaments is faster initially and slower later on when compared to Newtonian filaments [73]. Figure 10 shows that when α is lowered (to 0.1), such an observation is seen with a Giesekus filament (i.e., faster initial necking and slower necking later on), but only up to some intermediate strain, after which the rate of necking in it is higher than that of the Newtonian filament. In the Oldroyd-B limit ($\alpha = 0$), however, the rate of deformation of these filaments does not overtake that of the Newtonian filaments once they slow down (in fact, they never breakup) as in [73].

In elongational flows the dimensionless transient Trouton ratio Tr is defined as [74]

$$Tr = \frac{\tau_{zz} + \sigma_{zz} - \tau_{rr} - \sigma_{rr}}{\eta_0 \, \dot{\varepsilon}} \tag{24}$$

The transient Trouton ratio quantifies the resistance to the elongational flow; higher Tr indicates higher resistance to the flow. In the present analysis, a local Trouton ratio is computed at the mid-filament plane for different Ca (hereafter referred simply as Tr). The effective strain rate, $\dot{\varepsilon}_{\text{eff}}$, is used in

computing Tr, which is defined as [26]

$$\dot{\varepsilon}_{\text{eff}} = -2 \left(\frac{(v_r)_{\text{free surface}}}{R} \right)_{\text{mid-filament}} \tag{25}$$

$\dot{\varepsilon}_{\text{eff}}$ is substituted for $\dot{\varepsilon}$ in Eq. 24 to compute Tr. Figure 11 shows the variation of Tr in the radial direction at the mid-filament plane for different times. Tr is found to be roughly uniform along the cross-section at all times. Thus, the average (across the cross-section) and the point values of Tr at the free surface in the mid-filament plane are very close. Hereafter, only point values of Tr are reported. Figure 12 shows the variation of the transient Tr with the effective strain ε_{eff}. Clearly, the evolution of Tr depends on Ca; the curves for capillary numbers smaller than 1 show a marked departure from those for $Ca > 1$. The lower values of Tr explain the lesser resistance to elongation (as a consequence, more drastic necking) shown by the low Ca Giesekus filaments. Yao *et al.* [26, 27] have computed the transient Tr at higher values of Ca and shown that its evolution is independent of Ca. Here, we show that the transient Tr indeed depends on Ca and this dependence becomes important when $Ca < 1$. The variation of the transient Tr with the effective strain ε_{eff} in a uni-axial elongational flow (ideally what is aimed to be achieved in filament stretching rheometers) is also shown in Fig. 12. It can be seen that the computed variation of Tr with ε_{eff} for $Ca \geq 2$ matches quite well the prediction based on the ideal theory. This observation accords with earlier studies that have shown that filament stretching rheometers are more useful at high capillary numbers (see, e.g., [24, 26]).

4.3.2 Elastic effects on Giesekus filaments

The effects of elasticity on the dynamics of Giesekus filaments is studied by fixing $Ca = 0.1$ and varying De. Figure 13 shows the necking of Giesekus filaments at $De = 0$, 1, 2, 3, and 4. It can be observed that at higher De, filaments neck faster. The filament with $De = 4$ shows the most drastic necking

amongst all the filaments. Figure 14 shows the variation of the transient Tr with Hencky strain ε; Tr approaches the same steady value in all three filaments with different De. At smaller Hencky strains, the filament with $De = 4$ has the lowest value of Tr and the filament with $De = 1$ has the highest value. At higher Hencky strains (≥ 1), however, all filaments display comparable Tr values. The filaments approach breakup when ε is about 1.2 (evident from Fig. 13); therefore, computations of Tr do not proceed much beyond this value of strain. The difference in the necking behavior at these strains can be explained by the amount of *elastic unloading* or *elastic recoil* taking place near the end plates. Yao *et al.* [26, 27] have studied such elastic unloading effects. Their analysis of the kinematics near the end plates uses the sign of the axial component of the rate of strain tensor (D_{zz}) as an indicator of elastic recoil (negative D_{zz} implies recoil). Here we analyze elastic unloading by examining how the elastic stress tensor acts upon the rate of strain tensor. D_{zz} results are also included and the two analyses are compared.

In the equation of mechanical energy, the term $\mathbf{T} : \boldsymbol{\nabla}\mathbf{v}$ quantifies the conversion of the mechanical energy into internal energy. In incompressible Newtonian liquids, this term is always positive and gives the *dissipation* of the mechanical energy into internal energy [75]. In polymeric liquids, however, this term is not always positive.

The velocity gradient $\boldsymbol{\nabla}\mathbf{v}$ can be decomposed into the symmetric rate-of-strain tensor and anti-symmetric vorticity tensor, viz. $\boldsymbol{\nabla}\mathbf{v} = \mathbf{D} + \mathbf{W}$. The term for the conversion of the mechanical energy into internal energy is then $\mathbf{T} : (\mathbf{D} + \mathbf{W}) = \mathbf{T} : \mathbf{D}$ since $\mathbf{T} : \mathbf{W} = \mathbf{0}$ because $\mathbf{T}$ is symmetric and $\mathbf{W}$ is skew-symmetric. Using Eq. 3 and that $\mathbf{I} : \mathbf{D} = \operatorname{tr}\mathbf{D} = 0$ in incompressible flows gives

$$\mathbf{T} : \mathbf{D} = (\boldsymbol{\tau} + \boldsymbol{\sigma}) : \mathbf{D} \tag{26}$$

The term $\boldsymbol{\tau} : \mathbf{D}$ is always positive ($\boldsymbol{\tau} = 2\eta_s\mathbf{D}$ and $\mathbf{D} : \mathbf{D} > 0$) and represents viscous dissipation. The term $\boldsymbol{\sigma} : \mathbf{D}$ can be positive or negative; this is the reason why Eq. 6 holds [57, 76]. It is positive when the flow acts on the polymer molecules (the Helmholtz free energy grows) and negative when the polymer molecules act on the flow, i.e., when elastic unloading takes place (the Helmholtz free energy decreases). Thus, elastic unloading takes place in the flow domain wherever $\boldsymbol{\sigma} : \mathbf{D}$ is negative. Physically, when $\boldsymbol{\sigma} : \mathbf{D} < 0$, the elastic stresses work by pulling the fluid in axially and pushing it out radially; thus, the molecules *recoil* from a stretched state.

Figure 15 (a) shows the contour plots of $\boldsymbol{\sigma} : \mathbf{D}$ for $De = 1$ and $De = 3$ at Hencky strains $\varepsilon = 1.02$ and $\varepsilon = 1.04$, respectively. The dark blue regions in the plots correspond to the regions where $\boldsymbol{\sigma} : \mathbf{D} < 0$. In both filaments there are regions near the end plates where $\boldsymbol{\sigma} : \mathbf{D} < 0$ indicating the occurrence of elastic recoil there. The computations reveal that the extent of the regions with $\boldsymbol{\sigma} : \mathbf{D} < 0$ is larger when $De = 3$. The minimum value of $\boldsymbol{\sigma} : \mathbf{D}$, $(\boldsymbol{\sigma} : \mathbf{D})_{\min}$, is -46.5 when $De = 1$ and is -132.78 when $De = 3$. This clearly indicates that the magnitude of recoil is larger when $De = 3$ than when $De = 1$.

Figure 15 (b) shows the variation of $-(\boldsymbol{\sigma} : \mathbf{D})_{\min}$ at different De with Hencky strain ε. At a given strain, except at very small values of ε, $(\boldsymbol{\sigma} : \mathbf{D})_{\min}$ decreases ($-(\boldsymbol{\sigma} : \mathbf{D})_{\min}$ increases) as De increases (e.g., see inset for the variation of $(\boldsymbol{\sigma} : \mathbf{D})_{\min}$ with De at $\varepsilon = 1$). For Hencky strains greater than one, in which case the variation in Tr with De is negligible, a steep decrease in $(\boldsymbol{\sigma} : \mathbf{D})_{\min}$ with increase in De is observed. This indicates more pronounced elastic recoil in filaments with higher De. Because the capillary number is constant and the Trouton ratios are comparable here, the dynamics in these filaments differ only in the extent of elastic recoil. This suggests a strong correlation between thinning of filaments and the enhancement of elastic unloading in them.

Figure 16 shows the axial velocity profile along the axis of symmetry for three filaments with $De = 1$, 2, and 3 at a Hencky strain of about 1. The axial velocity decreases along the axis near the end plates, i.e., D_{zz} becomes negative there. Figure 17 (a) shows the variation of D_{zz} for these three viscoelastic filaments and also a Newtonian filament along the axis of symmetry. The filament with highest elasticity ($De = 3$) has the lowest value of D_{zz}. This shows that the amount of elastic unloading, according to the kinematic argument as well, increases with De. Figure 17 (b) shows in the same plot the variation of D_{zz} and of $\boldsymbol{\sigma} : \mathbf{D}$ along the axis of symmetry at $De = 3$. Elastic unloading near the end plate can be evinced from both kinematic (sign of D_{zz}) and energy (sign of $\boldsymbol{\sigma} : \mathbf{D}$) arguments. However, the extent of the recoil region predicted by the two arguments differs. Whereas the energy argument shows the molecules recoiling only in a small region near the end plates, the kinematic argument indicates recoil all the way to the end plates. Thus, even though $D_{zz} < 0$ close to the end plates, reduction in the free energy does not occur there (however, the extent of the region in which $\boldsymbol{\sigma} : \mathbf{D} < 0$ is broader and closer to the end plates away from the axis of symmetry as shown in Fig. 15 (a)). Moreover, the negative sign of D_{zz} is not always a result of the recoil of molecules but can also be caused by capillary forces as revealed in Fig. 17 (a) by the variation of D_{zz} along the axis of symmetry of a Newtonian filament. Therefore, the energy criterion is a more reliable indicator of recoil than the kinematic one.

4.3.3 Giesekus vs. the other models

Necking behavior in FENE-CR and FENE-P filaments is investigated and compared with that in an equivalent Giesekus filament. The extensibility parameter b in the FENE models is chosen such that it gives the same maximum extensional viscosity as the Giesekus model. The two FENE models were selected because both of them have bounded extensional viscosity like Giesekus,

their maximum extensional viscosity can be matched easily by adjusting b, and for a given b, FENE-CR and FENE-P models have the same maximum extensional viscosity [11, 77]. The mobility parameter in the Giesekus model α is set to 0.1 and b is set to 4 in the two FENE models. The elasticity is fixed in the calculations by setting $De = 2$ in all models.

Figure 18 shows the comparison of necking in these three filaments and an equivalent Newtonian filament at $Ca = 0.1$ and 2. The Giesekus filament shows the fastest and the most drastic necking among all filaments at these capillary numbers. Thinning behaviors of FENE-P and FENE-CR filaments are nearly indistinguishable. This is understandable, because in extensional flows both these models have similar transient extensional viscosity [77], although in shear flows they have different responses (FENE-CR has a constant shear viscosity whereas FENE-P is shear thinning). Hereafter, the dynamics of Giesekus filaments is compared only to that of FENE-CR filaments as the responses of the two FENE models are virtually the same.

Figure 19 shows the evolution of the transient Trouton ratio for Giesekus and FENE-CR filaments with Hencky strain. Both curves approach a comparable maximum value as is expected because the steady state extensional viscosities are close (it should be noted that calculations with the Giesekus model do not proceed beyond $\varepsilon \sim 1.2$ because the filament approaches breakup around this value of strain as explained in Sec. 4.3.2). The difference in the necking behavior of Giesekus and FENE models can be rationalized by the magnitude of elastic recoil taking place near the end plates. Figure 20 shows the value of $\boldsymbol{\sigma} : \mathbf{D}$ along the axis of symmetry for Giesekus and FENE-CR filaments at Hencky strains of $\varepsilon \sim 0.6$ (Fig. 20 (a)) and $\varepsilon \sim 0.8$ (Fig. 20 (b)). The Giesekus filament starts recoiling near the end plates at $\varepsilon \sim 0.8$ whereas the FENE-CR filament does not. Elastic recoil is seen in the FENE-CR filament at higher strains. The early onset and higher elastic recoil in the Giesekus filament thus appear to be related to its faster necking when compared to the

FENE-CR filament.

5 Concluding remarks

A new transient viscoelastic solver based on the earlier DEVSS-TG/SUPG mixed finite element algorithm and second-order predictor-corrector time integration scheme is presented. The general conformation tensor model, which allows easy implementation of different types of differential constitutive equations, is incorporated. The algorithm uses a fully coupled solver with elliptic mapping method. Consequently, it can handle complex physics such as overturning or folding of interfaces at low capillary number just before breakup.

The dynamics of weakly strain hardening viscoelastic liquid filaments, particularly those modeled by the Giesekus, FENE-CR, and FENE-P constitutive equations and subjected to elongational flows, is investigated. Giesekus filaments show the most drastic necking amongst the three filaments and their Newtonian counterpart. The evolution of the local transient Trouton ratio in the mid-filament plane for Giesekus filaments depends on the capillary number; this dependence becomes significant at $Ca < 1$. Moreover, for the same capillary number, Giesekus filaments with different Deborah number show different dynamics. The filaments with higher Deborah numbers deform more or neck faster. The faster necking with increase in Deborah number is demonstrated to correlate well with increased elastic unloading taking place near the end plates. The analysis of the elastic unloading based on the kinematics as well as on the action of the polymer molecules on the flow is presented. It is shown that the kinematic analysis can yield erroneous conclusions when capillary number is small.

Giesekus filaments have been shown to neck faster compared to FENE-CR and FENE-P filaments with comparable maximum steady extensional viscos-

ity. The difference in necking appears to be related to the difference in the elastic unloading near the end plates, which occurs earlier in Giesekus filaments.

In a recent publication, Matallah *et al.* [28] have observed the formation of a bead like structure in their simulations of stretching filaments modeled by the Phan-Thien/Tanner (PTT) viscoelastic constitutive equation with non-affine motion [78]. The PTT equation in this situation involves the Gordon-Schowalter (GS) convected derivative [79]. By contrast, the three viscoelastic constitutive equations studied in the present paper do not give rise to bead formation over the range of the parameters investigated. A noteworthy difference between the present paper and that of Matallah *et al.* [28] is that none of the constitutive equations used here involves the GS convected derivative. We have investigated in detail this starkly different behavior that may be observed during the stretching of filaments modeled by the PTT equation and have shown that bead formation in this case is due to the use of a constitutive equation that involves the GS convected derivative. The results of this analysis will be reported in a future publication [80].

Acknowledgments

This work was supported by the National Science Foundation (CTS-CAREER-0134389 and CTS-ITR-0312764) and by gifts from Rohm and Haas company to MP. OAB thanks the US DOE for support. Computational resources were provided by the Rice Terascale Cluster funded by NSF under Grant EIA-0216467, Intel, and HP. We thank X. Xie, M. Bajaj, and D. Arora for useful discussions that helped in the development of the transient solver.

References

[1] In S. F. Kistler and P. M. Schweizer, editors, *Liquid Film Coating*. Chapman & Hall, London, 1997.

[2] O. A. Basaran. Small-scale free surface flows with breakup: Drop formation and emerging applications. *AIChE J.*, 48:1842–1848, 2002.

[3] C. H. Park, H. J. Jeong, J. J. Jung, G. Y. Lee, S. C. Kim, T. S. Kim, S. H Yang, H. C. Chung, and S. Y. Rha. Fabrication of high quality cDNA microarray using a small amount of cDNA. *Int. J. Mol. Med.*, 13: 675–679, 2004.

[4] J. T. Yang, K. J. Huang, and A. C. Chen. Microfabrication and laser diagnosis of pressure-swirl atomizers. *J. Microelectromech. Sys.*, 13:843–850, 2004.

[5] A. U. Chen and O. A. Basaran. A new method for significantly reducing drop radius without reducing nozzle radius in drop-on-demand drop production. *Phys. Fluids*, 14:L1–L4, 2002.

[6] J. J. Cooper-White, J. E. Fagan, V. Tirtaatmadja, D. R. Lester, and D. V. Boger. Drop formation dynamics of constant low-viscosity, elastic fluids. *J. Non-Newtonian Fluid Mech.*, 106:29–59, 2002.

[7] J. Eggers. Drop formation - an overview. *Zamm-Z. Angew. Math. Me.*, 85:400–410, 2005.

[8] F. T. Trouton. On the coefficient of viscous traction and its relation to that of viscosity. *Proc. R. Soc. London Ser. A*, 77:426–440, 1906.

[9] M. Goldin, H. Yerushalmi, R. Pfeffer, and R. Shinnar. Breakup of a laminar capillary jet of a viscoelastic fluid. *J. Fluid Mech.*, 38:689–711, 1969.

[10] M. S. N. Oliveira and G. H. McKinley. Iterated stretching and multiple breads-on-a-string phenomena in dilute solutions of highly extensible flexible polymers. *Phys. Fluids*, 17:071704, 2005.

[11] R. A. Bird, C. F. Curtiss, R. C. Armstrong, and O. Hassager. *Dynamics of Polymeric Liquids*, volume 2. John Wiley & Sons, New York, 2nd edition, 1987.

[12] V. M. Entov and E. J. Hinch. Effect of a spectrum of relaxation times on the capillary thinning of a filament of elastic liquid. *J. Non-Newtonian Fluid Mech.*, 72:31–53, 1997.

[13] G. G. Fuller, C. A. Cathey, B. Hubbard, and B. E. Zebrowski. Extensional viscosity measurements for low-viscosity fluids. *J. Rheol.*, 31:235–249, 1987.

[14] P. Dontula, M. Pasquali, L. E. Scriven, and C. W. Macosko. Can extensional viscosity be measured with opposed nozzle devices? *Rheol. Acta*, 36:429–448, 1997.

[15] A. V. Bazilevskii, V. M. Entov, and A. N. Rozhkov. Liquid filament microrheometer and some of its applications. In D. R. Oliver, editor, *Third European Rheology Conference*, Elsevier, New York, 1990.

[16] G. H. McKinley and A. Tripathi. How to extract the Newtonian viscosity from capillary breakup measurements in a filament rheometer. *J. Rheol*, 44, 2000.

[17] J. E. Matta and R. P. Tytus. Liquid stretching using a falling cylinder. *J. Non-Newtonian Fluid Mech.*, 35:215–229, 1990.

[18] T. Sridhar, V. Tirtaatmadja, D. A. Nguyen, and R. K. Gupta. Measurement of extensional viscosity of polymer solutions. *J. Non-Newtonian Fluid Mech.*, 40:271–280, 1991.

[19] P. Szabo. Transient filament stretching rheometer I: Force balance analysis. *Rheol. Acta*, 36:277–284, 1997.

[20] G. H. McKinley and T. Sridhar. Filament-stretching rheometry of complex fluids. *Annu. Rev. Fluid Mech.*, 34:375–415, 2002.

[21] R. W. G. Shipman, M. M. Denn, and R. Keunings. Mechanics of the "falling plate" extensional rheometer. *J. Non-Newtonian Fluid Mech.*, 40:281–288, 1991.

[22] M. I. Kolte, H. K. Rasmussen, and O. Hassager. Transient filament stretching rheometer II: Numerical simulation. *Rheol. Acta*, 36:285–302, 1997.

[23] M. Yao and G. H. McKinley. Numerical simulation of extensional deformations of viscoelastic liquid bridges in filament stretching devices. *J. Non-Newtonian Fluid Mech.*, 74:47–88, 1998.

[24] R. Sizaire and V. Legat. Finite element simulation of a filament stretching extensional rheometer. *J. Non-Newtonian Fluid Mech.*, 71:89–107, 1997.

[25] X. Zhang, R. S. Padgett, and O. A. Basaran. Nonlinear deformation and breakup of stretching liquid bridges. *J. Fluid Mech.*, 329:207–245, 1996.

[26] M. Yao, G. H. McKinley, and B. Debbaut. Extensional deformation, stress relaxation and necking failure of viscoelastic filaments. *J. Non-Newtonian Fluid Mech.*, 79:469–501, 1998.

[27] M. Yao, S. H. Spiegelberg, and G. H. McKinley. Dynamics of weakly strain-hardening fluids in filament stretching devices. *J. Non-Newtonian Fluid Mech.*, 89:1–43, 2000.

[28] H. Matallah, M. J. Banaai, K. S. Sujatha, and M. F. Webster. Modelling filament stretching flows with strain-hardening models and sub-cell approximations. *J. Non-Newtonian Fluid Mech.*, 134:77–104, 2006.

[29] H. Giesekus. A simple constitutive equation for polymer fluids based on the concept of deformation-dependent tensorial mobility. *J. Non-Newtonian Fluid Mech.*, 11:69–109, 1982.

[30] A. C. Papanastasiou, L. E. Scriven, and C. W. Macosko. An integral constitutive equation for mixed flows: viscoelastic characterization. *J. Rheol.*, 27:387–410, 1983.

[31] O. Hassager, M. I. Kolte, and M. Renardy. Failure and nonfailure of fluid filaments in extension. *J. Non-Newtonian Fluid Mech.*, 76:137–151, 1998.

[32] K. Foteinopoulou, V. G. Mavrantzas, and J. Tsamopoulos. Numerical simulation of bubble growth in Newtonian and viscoelastic filaments undergoing stretching. *J. Non-Newtonian Fluid Mech.*, 122:177–200, 2004.

[33] K. Foteinopoulou, V. G. Mavrantzas, Y. Dimakopoulos, and J. Tsamopoulos. Numerical simulation of multiple bubbles growing in a Newtonian liquid filament undergoing stretching. *Phys. Fluids*, 18:042106, 2006.

[34] H. A. Stone and L. G. Leal. The effects of surfactants on drop deformation and breakup. *J. Fluid Mech.*, 220:161–186, 1990.

[35] J. R. Lister and H. A. Stone. Capillary breakup of a viscous thread sorrounded by another viscous fluid. *Phys. Fluids*, 10:2758–2764, 1998.

[36] C. W. Hirt and B. D. Nichols. Volume of fluid (VOF) method for the dynamics of free boundaries. *J. Comp. Phys.*, 39:201–225, 1981.

[37] S. Osher and J. A. Sethian. Fronts propagating with curvature dependent speed: Algorithms based on Hamilton-Jacobi formulation. *J. Comp. Phys.*, 79:12–49, 1988.

[38] S. F. Kistler and L. E. Scriven. Coating flow theory by finite element and asymptotic analysis of the Navier-Stokes system. *Int. J. Numer. Methods Fluid.*, 4:207–229, 1984.

[39] K. N. Christodoulou and L. E. Scriven. Discretization of free surface flows and other moving boundary problems. *J. Comp. Phys.*, 99:39–55, 1992.

[40] P. A. Sackinger, P. R. Schunk, and R. R. Rao. A Newton-Raphson pseudo-solid domain mapping technique for free and moving boundary problems: a finite element implementation. *J. Comp. Phys.*, 125:83–103, 1996.

[41] V. F. de Almeida. Domain deformation mapping: Application to variational mesh generation. *SIAM J. Sci. Comput.*, 20:1252–1275, 1999.

[42] E. D. Wilkes, S. D. Phillips, and O. A. Basaran. Computational and experimental analysis of dynamics of drop formation. *Phys. Fluids*, 11: 3577–3558, 1999.

[43] A. U. Chen, P. K. Notz, and O. A. Basaran. Computational and experimental analysis of pinch-off and scaling. *Phys. Rev. Lett.*, 88:174501, 2002.

[44] P. K. Notz and O. A. Basaran. Dynamics and breakup of a contracting liquid filament. *J. Fluid Mech.*, 512:223–256, 2004.

[45] R. Suryo and O. A. Basaran. Local dynamics during pinch-off of liquid

threads of power law fluids: Scaling analysis and self-similarity. *J. Non-Newtonian Fluid Mech.*, 138:134–160, 2006.

[46] R. G. Owens and T. N. Phillips. *Computational Rheology.* Imperial College Press, London, 1st edition, 2002.

[47] F. P. T. Baaijens. Mixed finite element methods for viscoelastic flow analysis: a review. *J. Non-Newtonian Fluid Mech.*, 79:361–385, 1998.

[48] O. J. Romero, L. E. Scriven, and M. S. Carvalho. Slot coating of mildly viscoelastic liquids. *J. Non-Newtonian Fluid Mech.*, 138:63–75, 2006.

[49] M. Pasquali and L. E. Scriven. Free surface flows of polymer solutions with models based on conformation tensor. *J. Non-Newtonian Fluid Mech.*, 108:363–409, 2002.

[50] A. G. Lee, E. S. G. Shaqfeh, and B. Khomami. A study of viscoelastic free surface flows by the finite element method: Hele-Shaw and slot coating flows. *J. Non Newtonian Fluid Mech.*, 108:327–362, 2002.

[51] Y. Dimakopoulos and J. Tsamopoulos. On the gas-penetration in straight tubes completely filled with a viscoelastic fluid. *J. Non Newtonian Fluid Mech.*, 117:117–139, 2004.

[52] G. A. Zevallos, M. S. Carvalho, and M. Pasquali. Forward roll coating flows of viscoelastic liquids. *J. Non-Newtonian Fluid Mech.*, 130:96–109, 2005.

[53] H. K. Rasmussen and O. Hassager. Simulation of transient viscoelastic flow. *J. Non-Newtonian Fluid Mech.*, 46:289–305, 1993.

[54] O. G. Harlen, J. M. Rallison, and P. Szabo. A split Lagrangian-Eulerian method for simulating transient viscoelastic flows. *J. Non-Newtonian Fluid Mech.*, 60:81–104, 1995.

[55] A. Bach, H. K. Rasmussen, P-.Y. Longin, and O. Hassager. Growth of non-axisymmetric disturbances of the free surface in the filament stretching rheometer: experiments and simulation. *J. Non-Newtonian Fluid Mech.*, 108:163–186, 2002.

[56] M. D. Chilcott and J. M. Rallison. Creeping flow of dilute polymer solutions past cylinders and spheres. *J. Non-Newtonian Fluid Mech.*, 29: 381–432, 1988.

[57] M. Pasquali and L. E. Scriven. Theoretical modeling of microstructured liquids: a simple thermodynamic approach. *J. Non-Newtonian Fluid Mech.*, 120:101–135, 2004.

[58] M. Grmela and P. J. Carreau. Conformation tensor rheological models. *J. Non-Newtonian Fluid Mech.*, 23:271–294, 1987.

[59] A. N. Beris and B. J. Edwards. *Thermodynamics of Flowing Systems with Internal Microstructure.* Oxford University Press, Oxford, 1st edition, 1994.

[60] R. J. J. Jongschaap, K. H. de Haas, and C. A. J. Damen. A generic matrix representation of configuration tensor rheological models. *J. Rheol.*, 38: 769–796, 1994.

[61] J. M. de Santos. *Two-phase Cocurrent Downflow through Constricted Passages*. PhD thesis, University of Minnesota, Minneapolis, MN, 1991. Available from UMI, Ann Arbor, MI, order number 9119386.

[62] M. J. Szady, T. R. Salamon, A. W. Liu, R. C. Armstrong, and R. A. Brown. A new mixed finite element method for viscoelastic flows governed by differential constitutive equations. *J. Non-Newtonian Fluid Mech.*, 59: 215–243, 1995.

[63] R. Guénette and M. Fortin. A new finite element method for computing viscoelastic flows. *J. Non-Newtonian Fluid Mech.*, 60:27–52, 1995.

[64] M. Fortin. Old and new finite elements for incompressible flows. *Int. J. Numer. Meth. Fluids*, 1:347–364, 1981.

[65] P. M. Gresho, R. R. Lee, and R. C. Sani. On the time-dependent solution of the incompressible Navier-Stokes equations in two and three dimensions. In C. Taylor and K. Morgan, editors, *Recent Advances in Numerical Methods in Fluids*, volume 1, page 27, Pineridge Press, Swansea, UK, 1980.

[66] C. Bodart and M. Crochet. The time-dependent flow of a viscoelastic fluid around a sphere. *J. Non-Newtonian Fluid Mech.*, 54:303–329, 1994.

[67] M. Luskin and R. Rannacher. On the smoothing property of the Crank-Nicholson scheme. *Applicable Anal.*, 14:117–135, 1982.

[68] I. S. Duff, A. M. Erisman, and J. K. Reid. *Direct Methods for Sparse Matrices*. Oxford University Press, Oxford, 1st edition, 1989.

[69] P. K. Notz, A. U. Chen, and O. A. Basaran. Satellite drops: Unexpected dynamics and change of scaling during pinch-off. *Phys. Fluids*, 13:549–552, 2001.

[70] L. F. Richardson. The approximate arithmetical solution by finite differences of physical problems involving differential equations, with an application to the stresses in a masonary dam. *Phil. Trans. R. Soc. London Ser. A*, 210:307–357, 1911.

[71] J.-M. Li, W. R. Burghardt, B. Yang, and B. Khomami. Flow birefringence and computational studies of a shear thinning polymer solution in axisymmetric stagnation flow. *J. Non-Newtonian Fluid Mech.*, 74:151–193, 1998.

[72] M. Renardy. A numerical study of the asymptotic evolution and breakup of Newtonian and viscoelastic jets. *J. Non-Newtonian Fluid Mech.*, 59: 267–282, 1995.

[73] D. W. Bousfield, R. Keunings, G. Marrucci, and M. M. Denn. Nonlinear

analysis of the surface tension driven breakup of viscoelastic filaments. *J. Non-Newtonian Fluid Mech.*, 21:79–97, 1986.

[74] C. W. Macosko. *Rheology*. VCH, New York, 1st edition, 1994.

[75] R. B. Bird, W. E. Stewart, and E. N. Lightfoot. *Transport Phenomena*. John Wiley & Sons, New York, 1960.

[76] M. Pasquali. *Polymer Molecules in Free Surface Coating Flows*. PhD thesis, University of Minnesota, Minneapolis, MN, 2000. Available from UMI, Ann Arbor, MI, order number 9963019.

[77] M. Herrchen and H. C. Öttinger. A detailed comparison of various FENE dumbbell models. *J. Non-Newtonian Fluid Mech.*, 68:17–42, 1997.

[78] N. Phan-Thien and R. I. Tanner. A new constitutive equation derived from network theory. *J. Non-Newtonian Fluid Mech.*, 2:353–365, 1977.

[79] R. J. Gordon and W. R. Schowalter. Anisotropic fluid theory: A different approach to the dumbbell theory of dilute polymer solutions. *Trans. Soc. Rheol.*, 16:79–97, 1972.

[80] P. P. Bhat, O. A. Basaran, and M. Pasquali. To be submitted to *J. Non-Newtonian Fluid Mech.*, 2007.

Table 1
Constitutive functions in the general conformation tensor model [57] for different types of constitutive equations used in this paper. G is the elastic modulus, α is the mobility parameter in the Giesekus model ($0 \leq \alpha \leq 1$), I_M is the trace of the conformation tensor $\mathbf{M}$, and b is the extensibility parameter in the FENE models.

	$\xi(\mathbf{M})$	$\zeta(\mathbf{M})$	$g_0(\mathbf{M})$	$g_1(\mathbf{M})$	$g_2(\mathbf{M})$	$\frac{2\rho}{G}a(\mathbf{M})$
Oldroyd-B	1	1	-1	1	0	$I_M - 3$
Giesekus	1	1	$\alpha - 1$	$1 - 2\alpha$	α	$I_M - 3$
FENE-CR	1	1	$-\frac{b-1}{b-(I_M/3)}$	$\frac{b-1}{b-(I_M/3)}$	0	$3(b-1)\ln\frac{b-1}{b-(I_M/3)}$
FENE-P	1	1	-1	$\frac{b-1}{b-(I_M/3)}$	0	$3(b-1)\ln\frac{b-1}{b-(I_M/3)}$

Table 2
Comparison of the breakup length L_b/R_0 and the ratio (%) of the volume of the sessile drop to the total volume V_{sessile}/V for a linearly stretching Newtonian filament between this work (2-D) and that of Zhang *et al.* (1-D) [25]. The dimensionless numbers are $Re = 9.56$, $Ca = 8.2 \times 10^{-5}$, and $Bo = 0.342$.

	L_b/R_0	V_{sessile}/V
Zhang *et al.* [25]	3.665	87.94 %
This work	3.695	87.51 %

Table 3
The minimum neck radius $R_{\min}/R_0$ and the maximum value of the axial component of the conformation tensor along the free surface, $(M_{zz})_{\max}$, at Hencky strain $\varepsilon = 3$ obtained from calculations with the three meshes: Mesh 1, Mesh 2, and Mesh 3 (see text for details). The viscoelastic model is the Giesekus model and the parameters used in the calculations are $\Lambda_0 = 0.54$, $\alpha = 0.32$, $\beta = 0.262$, $Re = 0$, $Ca = 18.27$, and $De = 2$. Order of convergence from these results is obtained using Richardson extrapolation.

	Mesh 1	Mesh 2	Mesh 3	Order
$R_{\min}/R_0$	5.67327×10^{-2}	5.73302×10^{-2}	5.74659×10^{-2}	3.65
$(M_{zz})_{\max}$	37.21217	36.98751	36.92279	3.07

Table 4
The minimum neck radius $R_{\min}/R_0$ and the maximum value of the axial component of the conformation tensor along the free surface, $(M_{zz})_{\max}$, at Hencky strain $\varepsilon = 3$ obtained from calculations with the three time steps: $\Delta t_1 = 2{\times}10^{-3}$, $\Delta t_2 = 1{\times}10^{-3}$, and $\Delta t_3 = 5 \times 10^{-4}$. The viscoelastic model is Giesekus and the parameters used in the calculation are $\Lambda_0 = 0.54$, $\alpha = 0.32$, $\beta = 0.262$, $Re = 0$, $Ca = 18.27$, and $De = 2$. Second-order accuracy of the time integration method is verified from the fact that the calculated order of convergence is 2.06 in both instances.

	Δt_1	Δt_2	Δt_3	Order
$R_{\min}/R_0$	5.73336×10^{-2}	5.73302×10^{-2}	5.73294×10^{-2}	2.06
$(M_{zz})_{\max}$	36.98670	36.98751	36.98770	2.06

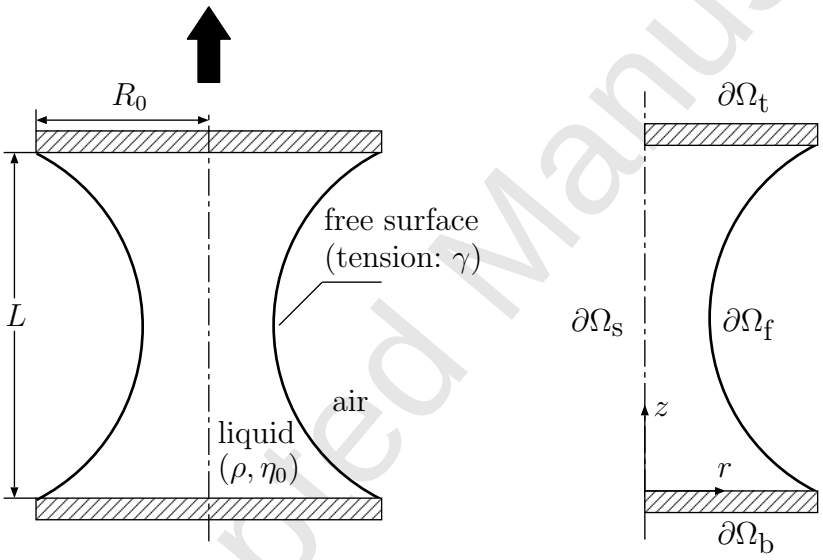

Fig. 1. Left: a schematic of a liquid bridge between a moving top plate and a stationary bottom plate. L is the length of the bridge and R_0 is the radius of the plate. Right: computational flow domain and boundaries.

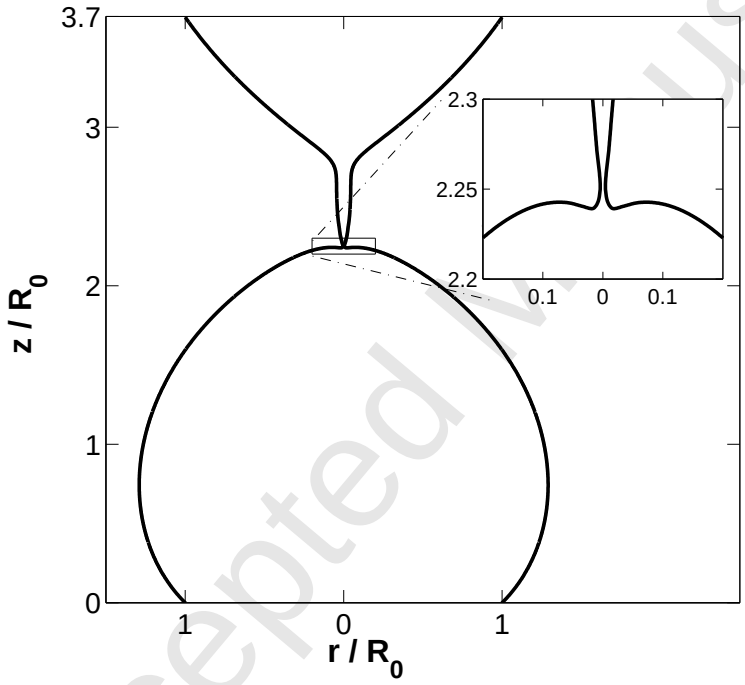

Fig. 2. Profile of a stretching Newtonian liquid bridge with $\Lambda_0 = 3$, $Re = 9.56$, $Bo = 0.342$, and $Ca = 8.2 \times 10^{-5}$ close to breakup. The inset shows the zoomed in view of the overturned interface.

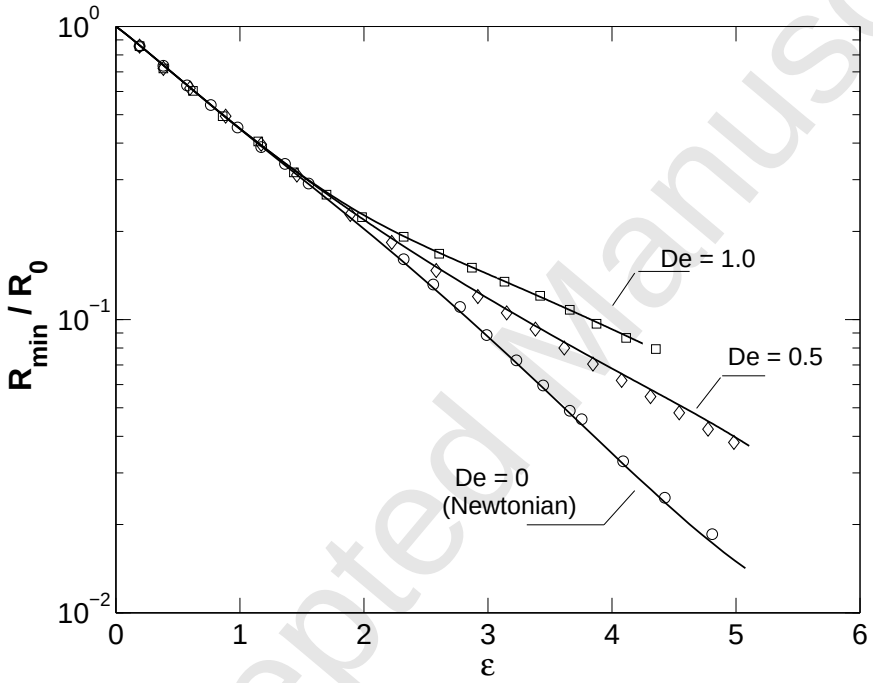

Fig. 3. Evolution of the minimum neck radius $R_{\min}/R_0$ in Newtonian and Oldroyd-B filaments with Hencky strain ε at $De = 0$ (Newtonian), 0.5 and 1. Results from this work are compared with that of YM [23]. Here, $\Lambda_0 = 1/3$, $Re = 0.0138$, $Ca = 63.26$, and $\beta = 0.915$ (Oldroyd-B). The solid lines are from this work and the symbols have been obtained from reading continuous lines in Fig. 7 of YM using `datathief`.

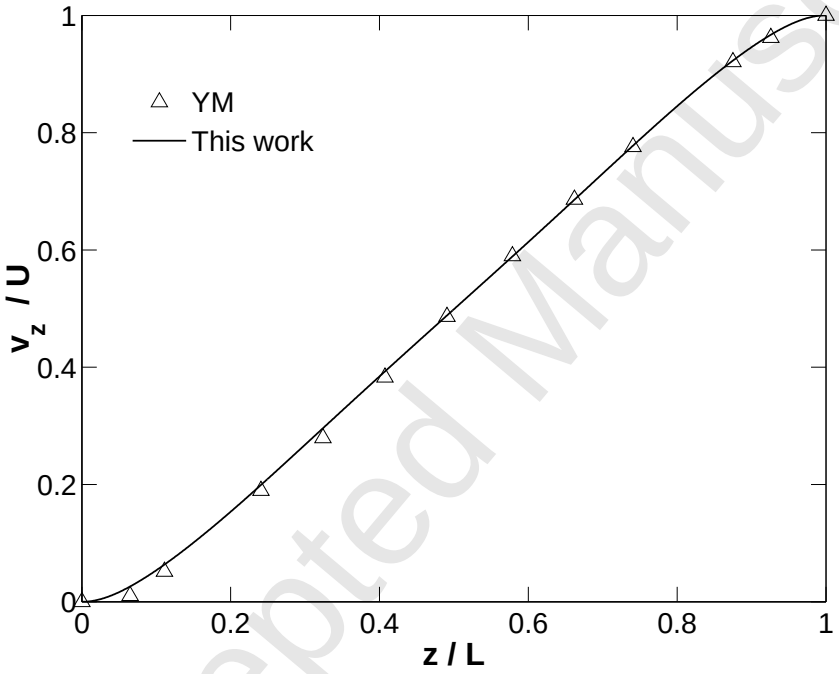

Fig. 4. Axial velocity normalized with the top plate velocity U along the axis of symmetry ($r = 0$). Results are compared with that of YM [23] at Hencky strain $\varepsilon = 2$. Here, $\Lambda_0 = 1/3$, $Re = 0.0138$, $Ca = 63.26$, $\beta = 0.915$, and $De = 5.1$ (Oldroyd-B). The solid lines are from this work and the symbols have been obtained from Fig. 9 of YM using `datathief`.

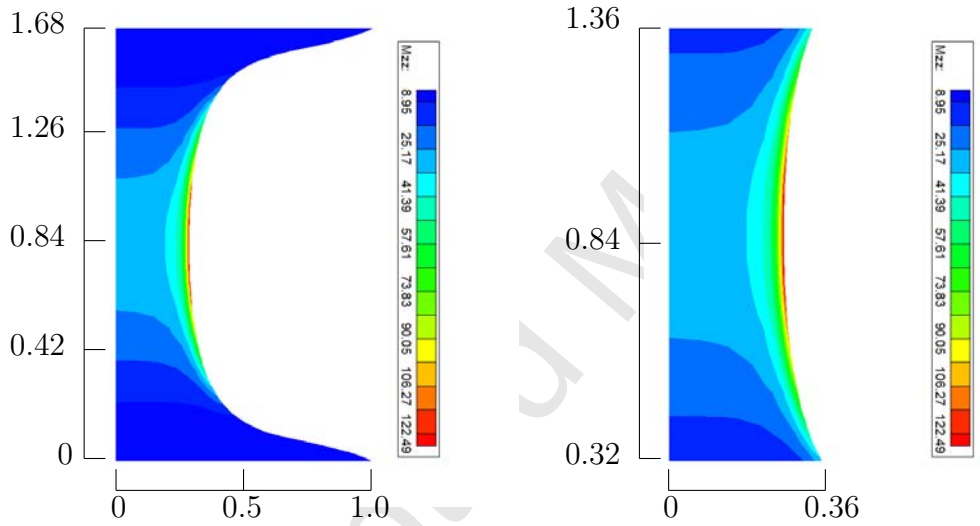

Fig. 5. Contours (colors online) of the axial component of the conformation tensor M_{zz} at Hencky strain $\varepsilon = 1.62$. Here, $\Lambda_0 = 1/3$, $Re = 0.0138$, $Ca = 63.26$, $\beta = 0.915$, and $De = 1$ (Oldroyd-B). Left: overall profile. Right: zoomed in view of the mid-filament region showing the existence of a thin boundary layer near the free surface.

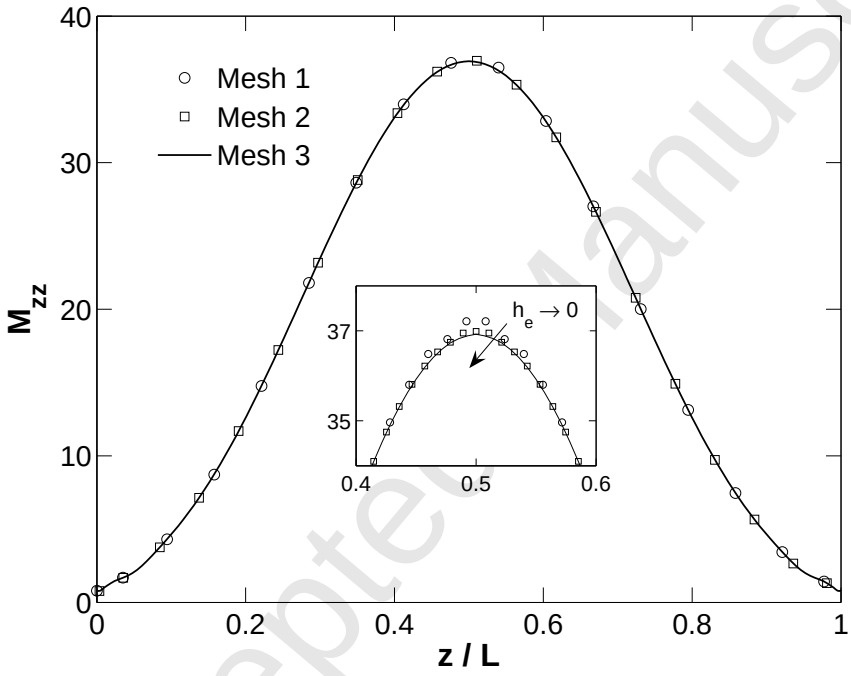

Fig. 6. Variation of the axial component of the conformation tensor M_{zz} along the free surface at Hencky strain $\varepsilon = 3$. Results are from computations with the three meshes: Mesh 1, Mesh 2, and Mesh 3 (see text for details). Giesekus filament with parameters $\alpha = 0.32$, $\beta = 0.262$, $\Lambda_0 = 0.54$, $Re = 0$, $Ca = 18.27$, and $De = 2$ is simulated. h_e is the characteristic element size.

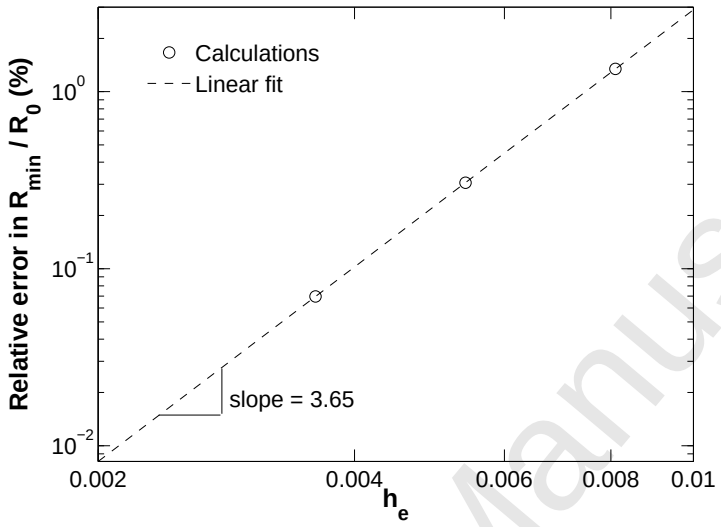

(a)

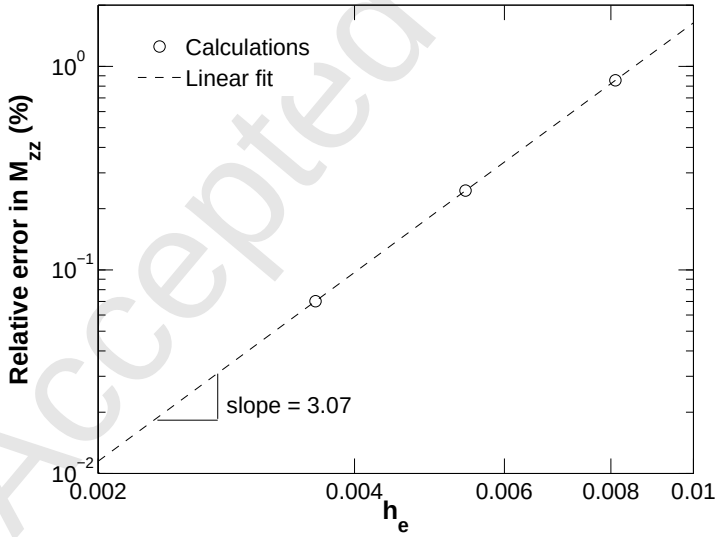

(b)

Fig. 7. Variation of the relative errors (see text for definition) in (a) $R_{\min}/R_0$ and (b) $(M_{zz})_{\max}$. The dashed lines are the linear fits; the slopes of these lines give the order of convergence, which is 3.65 in the former case and 3.07 in the latter case.

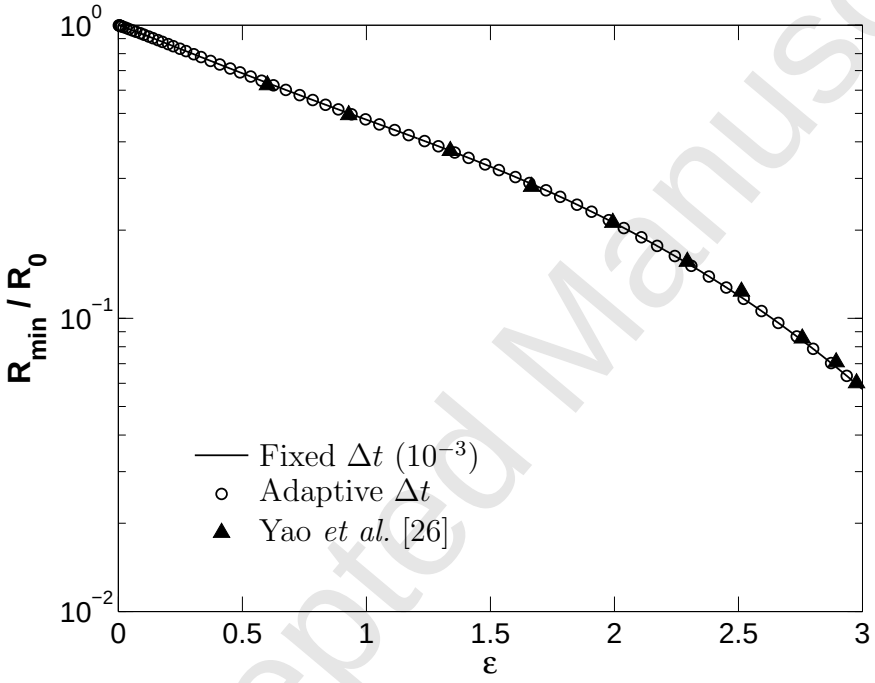

Fig. 8. Variation of the minimum neck radius $R_{\min}/R_0$ with Hencky strain ε. Calculations are performed with a fixed time step $\Delta t = 1 \times 10^{-3}$ (a total of 1500 time steps are required to reach $\varepsilon = 3$ at $\dot{\varepsilon}$= 2), and with adaptive time stepping (a total of 68 steps at same $\dot{\varepsilon}$ with average $\Delta t = 2.2 \times 10^{-2}$). Here, $\Lambda_0 = 0.54$, $\alpha = 0.32$ (Giesekus), $\beta = 0.262$, $Re = 0$, $Ca = 18.27$, and $De = 2$.

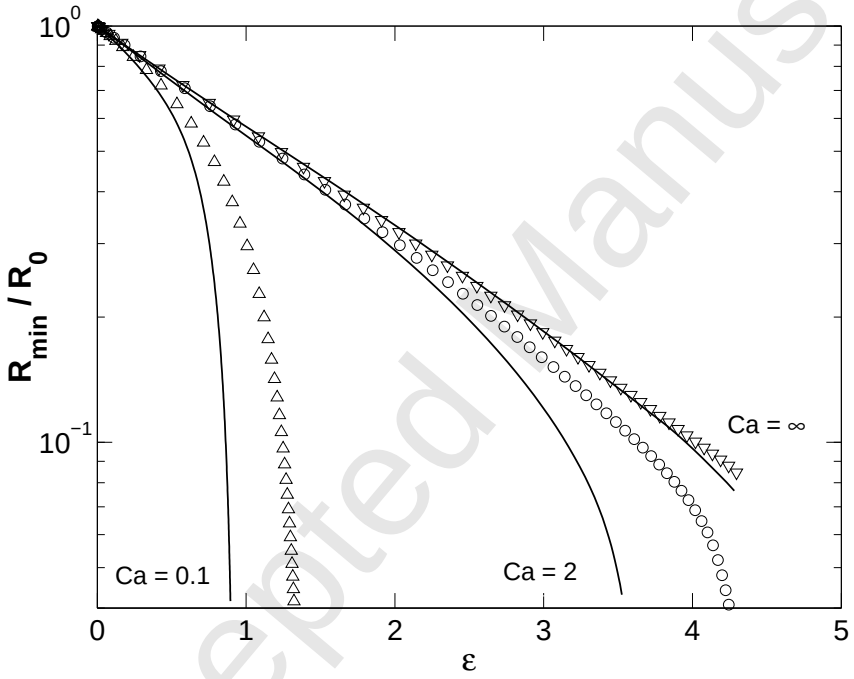

Fig. 9. Necking in Newtonian (symbols) and Giesekus filaments (lines) at $Re = 0$ and different Ca. The parameters in the Giesekus computations are $\alpha = 0.32$, $\beta = 0.262$, and $De = 2.0$.

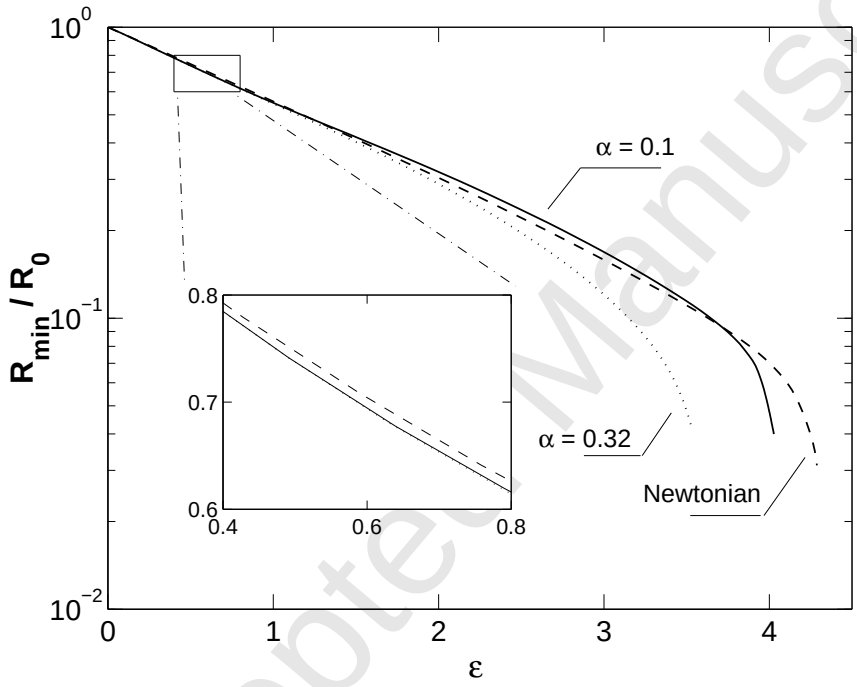

Fig. 10. Evolution of the minimum neck radius $R_{\min}/R_0$ with Hencky strain ε in Giesekus filaments. Here, $\beta = 0.262$, $De = 2.0$, $Re = 0$, and $Ca = 2.0$. Necking in the Giesekus filament is greater than its Newtonian counterpart when $\alpha = 0.32$. However, deformations in the Giesekus filament are larger at shorter times, smaller at intermediate times, and larger again at longer times, than the Newtonian filaments when $\alpha = 0.1$ (see inset for details on short time behavior).

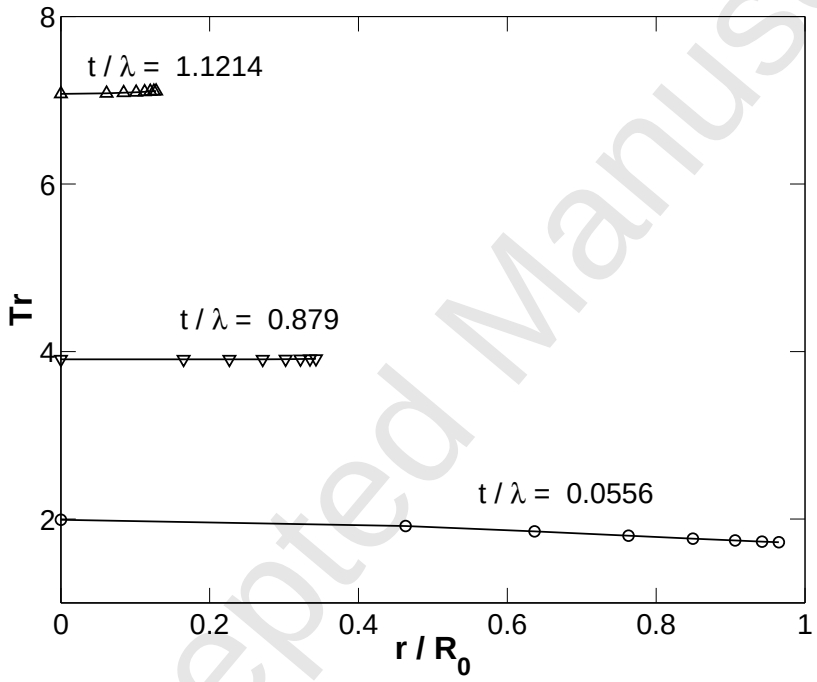

Fig. 11. Variation of the local transient Trouton ratio, Tr, in Giesekus filaments ($\alpha = 0.1$, $\beta = 0.6$) along the cross-section of the mid-plane at different times. The dimensionless numbers are $De = 1.0$, $Re = 0$, and $Ca = 0.1$. The filament initial aspect ratio $\Lambda_0 = 3$ in this and all the subsequent results shown.

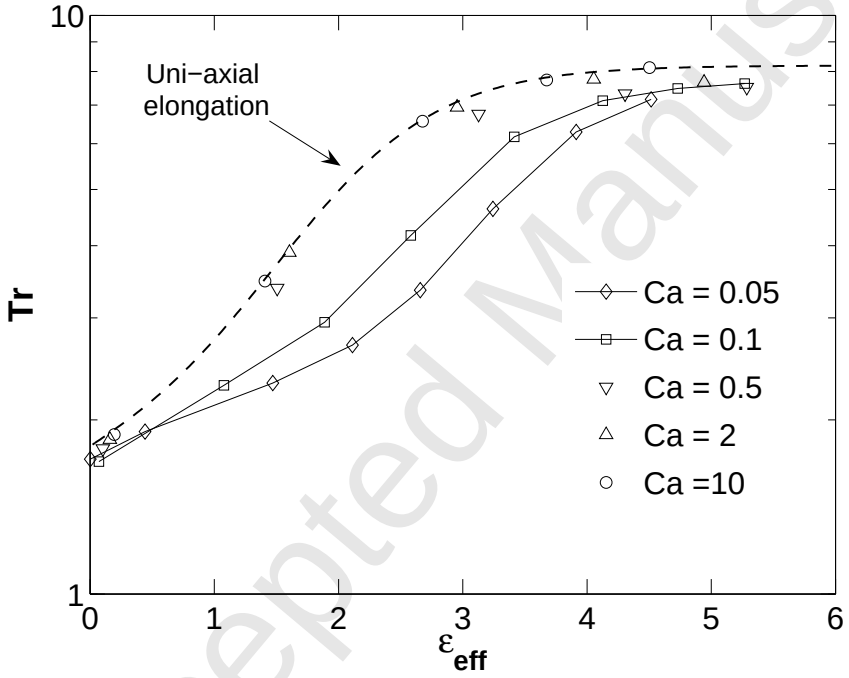

Fig. 12. Variation of the transient Trouton ratio Tr with effective strain ε_{eff} in Giesekus filaments ($\alpha = 0.1$, $\beta = 0.6$, $De = 2.0$, and $Re = 0$) at different Ca. The dashed line corresponds to the evolution of Tr in a uni-axial elongational flow.

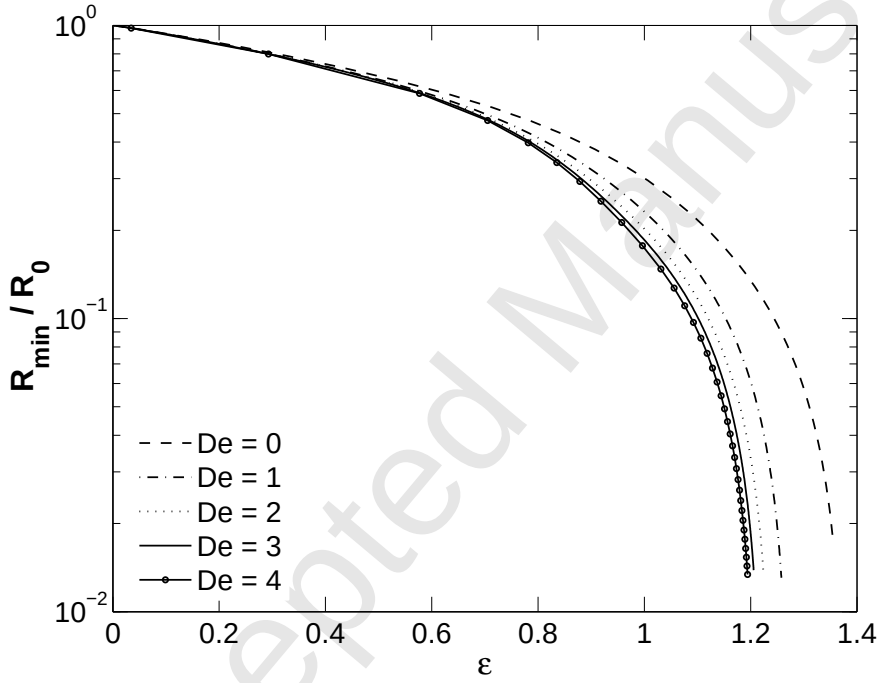

Fig. 13. Evolution of the minimum neck radius $R_{\min}/R_0$ with Hencky strain ε in Giesekus filaments ($\alpha = 0.1$, $\beta = 0.6$, $Ca = 0.1$, and $Re = 0$) at different values of De.

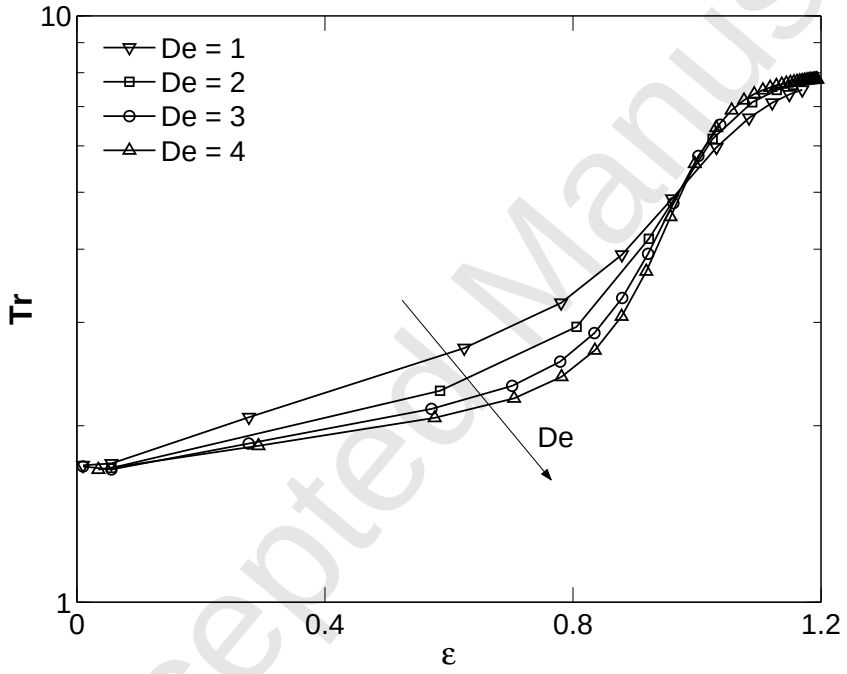

Fig. 14. Evolution of the transient Trouton ratio Tr with Hencky strain ε at different De in Giesekus filaments ($\alpha = 0.1$, $\beta = 0.6$, $Ca = 0.1$, and $Re = 0$) .

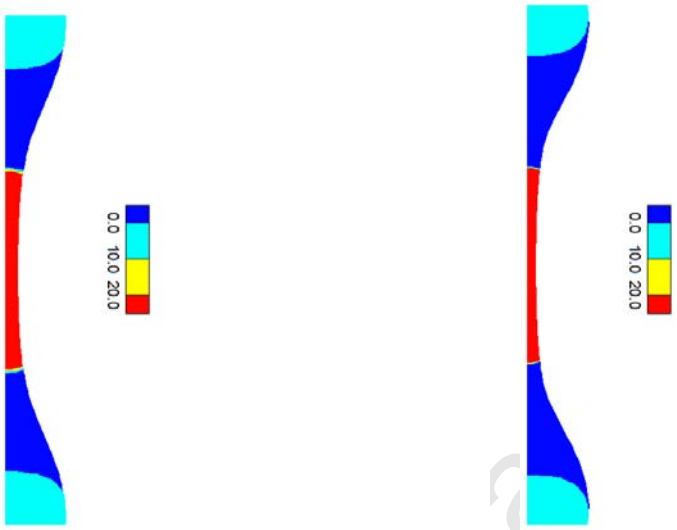

(a)

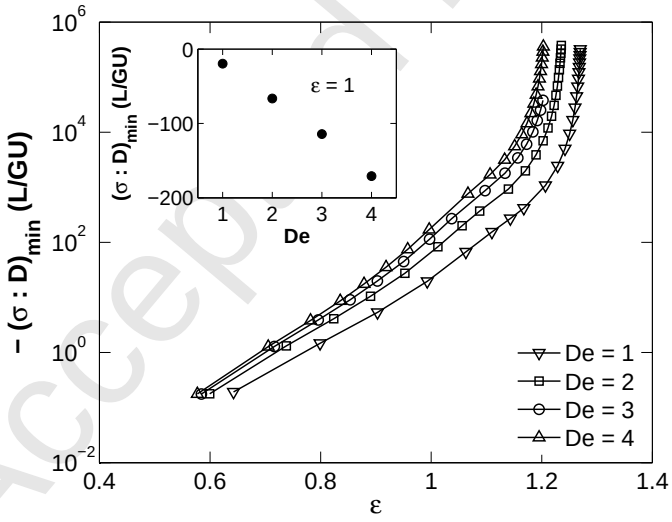

(b)

Fig. 15. (a) Contours (colors online) of $\boldsymbol{\sigma} : \mathbf{D}$ for Giesekus filaments. Left: $De = 1.0$ and $\varepsilon = 1.02$. Right: $De = 3.0$ and $\varepsilon = 1.04$. (b) Variation of normalized $-(\boldsymbol{\sigma} : \mathbf{D})_{\min}$ in Giesekus filaments with Hencky strain ε at different De. The inset shows normalized $(\boldsymbol{\sigma} : \mathbf{D})_{\min}$ as a function of De at Hencky strain $\varepsilon = 1$. In both (a) and (b), $\alpha = 0.1$, $\beta = 0.6$, $Ca = 0.1$, and $Re = 0$.

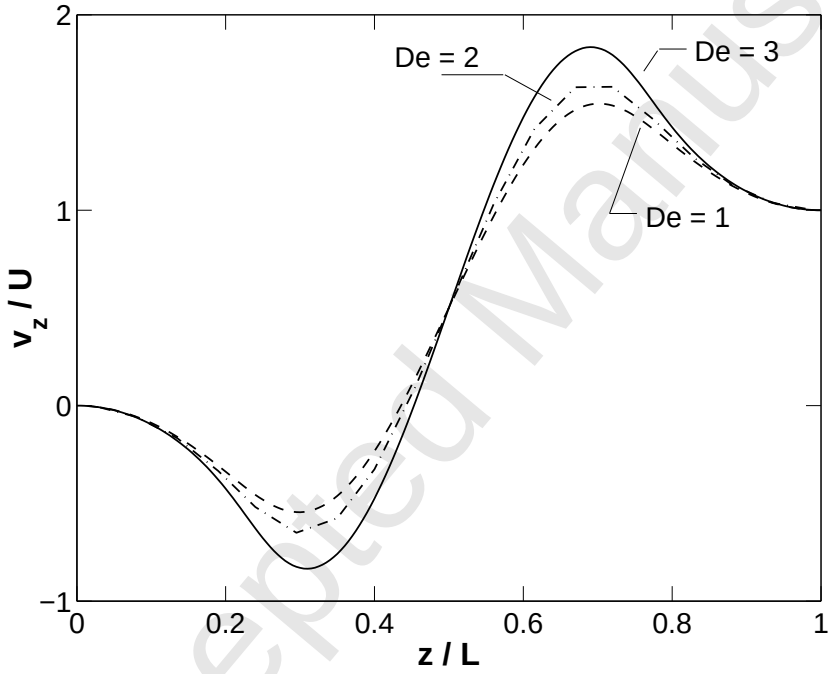

Fig. 16. Variation of the axial velocity v_z normalized with the top plate velocity U along the axis of symmetry ($r = 0$) in Giesekus filaments ($\alpha = 0.1$, $\beta = 0.6$, $Ca = 0.1$, and $Re = 0$) at different De and $\varepsilon \sim 1.0$.

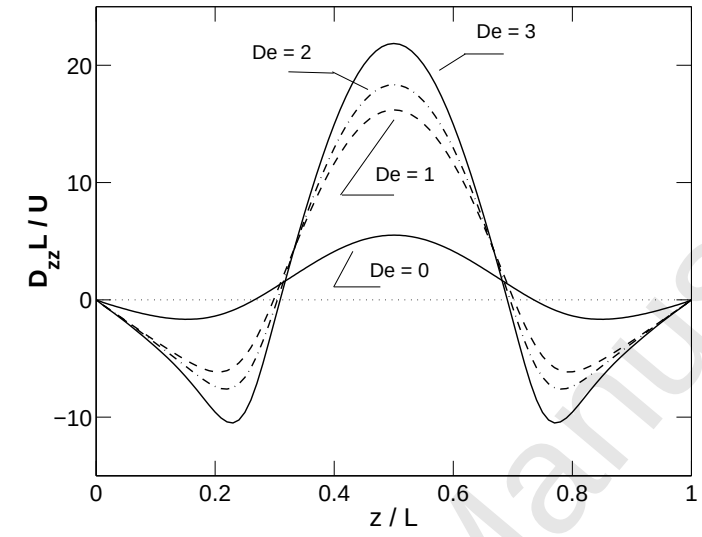

(a)

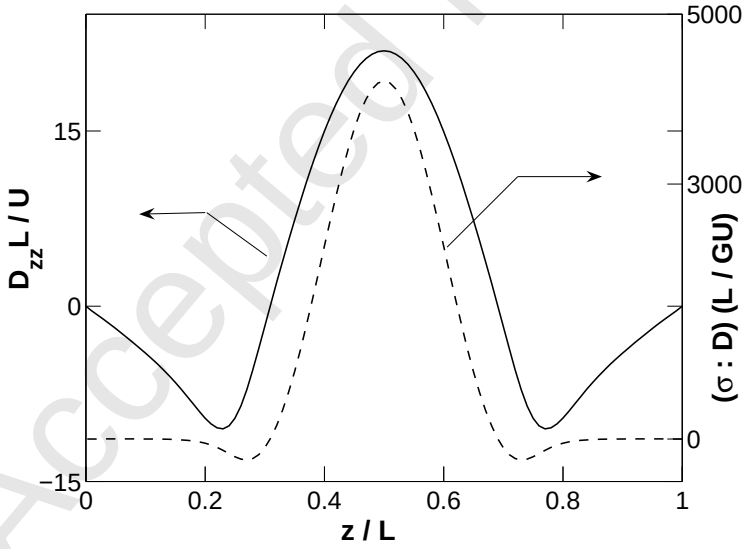

(b)

Fig. 17. (a) Variation of normalized D_{zz} along the axis of symmetry in Newtonian ($De = 0$) and Giesekus filaments ($\alpha = 0.1$, $\beta = 0.6$, and at different De). (b) Variation of normalized D_{zz} and normalized $\boldsymbol{\sigma} : \mathbf{D}$ along the axis of symmetry at $De = 3.0$. Here, $Ca = 0.1$, $Re = 0$, and $\varepsilon \sim 1.0$.

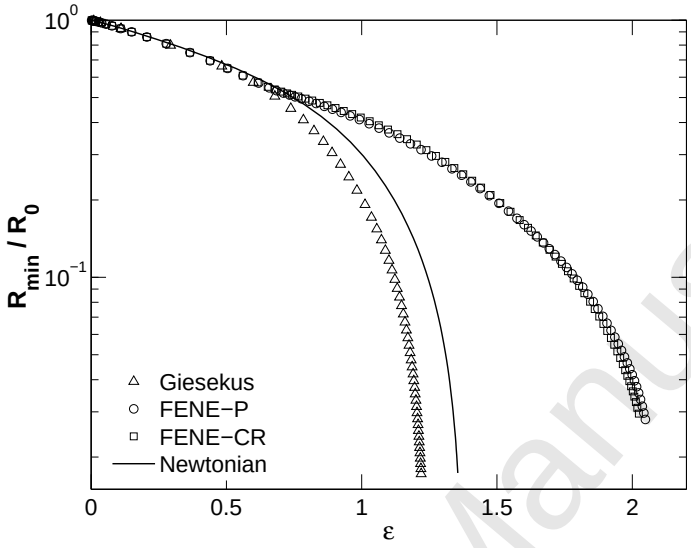

(a)

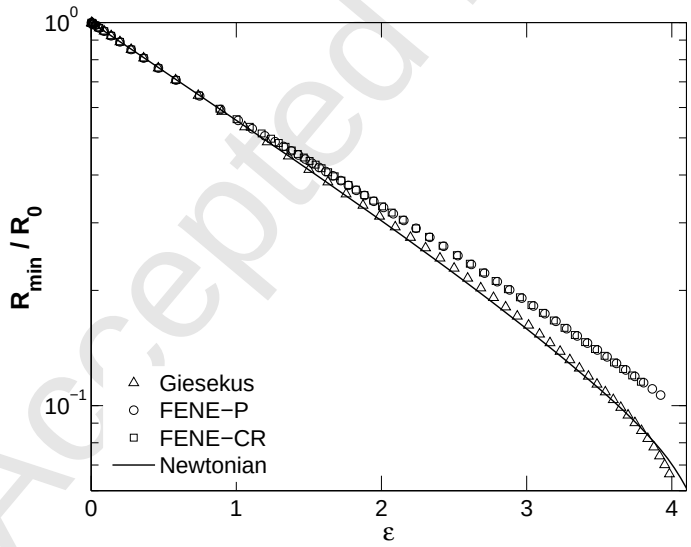

(b)

Fig. 18. Necking in the three viscoelastic filaments: Giesekus ($\alpha = 0.1$), FENE-CR ($b = 4$), FENE-P ($b = 4$), and an equivalent Newtonian filament. Here, $\beta = 0.6$, $Re = 0$, and $De = 2.0$. (a) $Ca = 0.1$ and (b) $Ca = 2.0$.

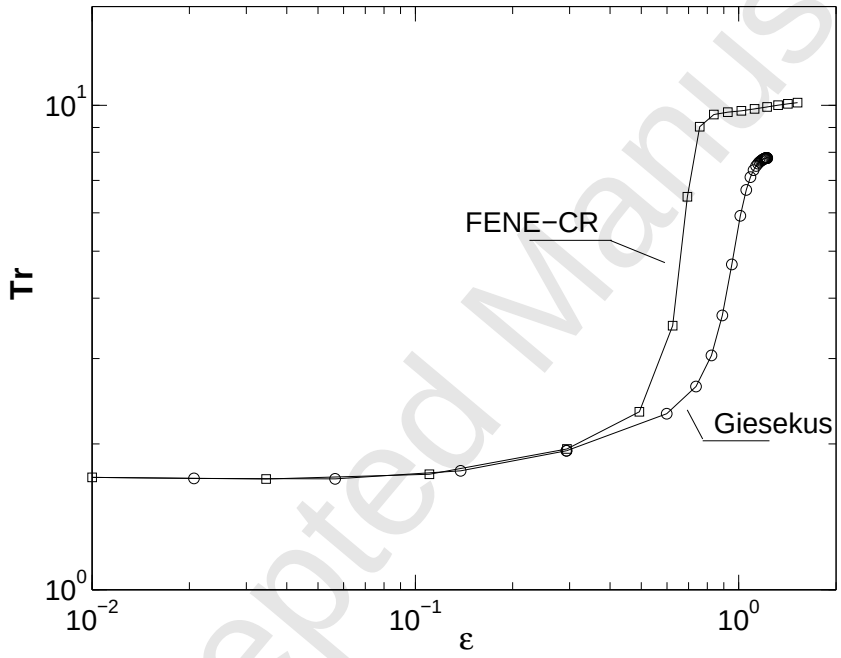

Fig. 19. Evolution of the transient Trouton ratio Tr with Hencky strain ε in Giesekus ($\alpha = 0.1$) and FENE-CR ($b = 4$) filaments. Here, $\beta = 0.6$, $De = 2.0$, $Re = 0$, and $Ca = 0.1$.

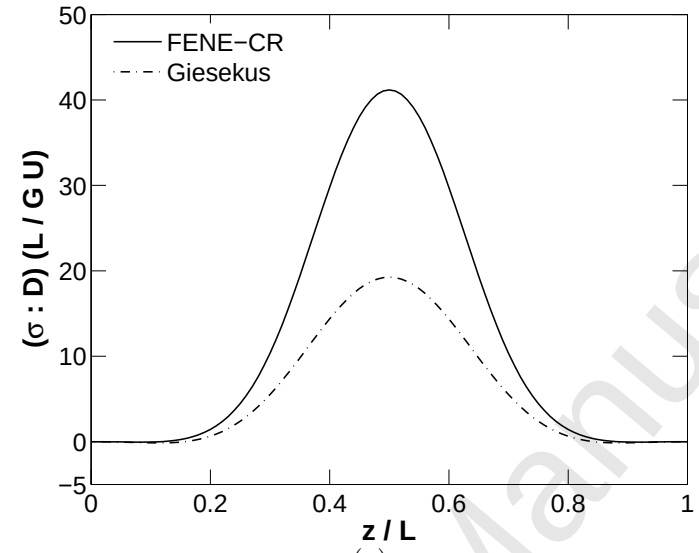

(a)

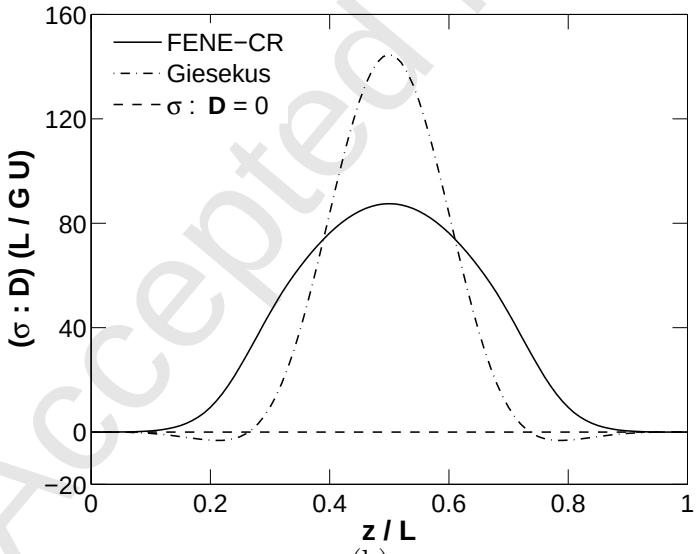

(b)

Fig. 20. Variation of normalized $\boldsymbol{\sigma} : \mathbf{D}$ along the axis of symmetry for Giesekus filaments ($\alpha = 0.1$) and FENE-CR filaments ($b = 4$). Here, $\beta = 0.6$, $Ca = 0.1$, $De = 2.0$, and $Re = 0$. (a) $\varepsilon = 0.59$ (Giesekus), $\varepsilon = 0.62$ (FENE-CR). (b) $\varepsilon = 0.81$ (Giesekus), $\varepsilon = 0.85$ (FENE-CR).